

## LAMINAR AND TURBULENT DYNAMOS IN CHIRAL MAGNETOHYDRODYNAMICS. II. SIMULATIONS

JENNIFER SCHOBER<sup>1,2</sup>, IGOR ROGACHEVSKI<sup>3,1,4</sup>, AXEL BRANDENBURG<sup>1,4,5,6</sup>, ALEXEY BOYARSKY<sup>7</sup>, JÜRIG FRÖHLICH<sup>8</sup>,  
OLEG RUCHAYSKIY<sup>9</sup>, AND NATHAN KLEEORIN<sup>3,1</sup>

<sup>1</sup>Nordita, KTH Royal Institute of Technology and Stockholm University, Roslagstullsbacken 23, 10691 Stockholm, Sweden

<sup>2</sup>Laboratoire d'Astrophysique, EPFL, CH-1290 Sauvigny, Switzerland

<sup>3</sup>Department of Mechanical Engineering, Ben-Gurion University of the Negev, P.O. Box 653, Beer-Sheva 84105, Israel

<sup>4</sup>Laboratory for Atmospheric and Space Physics, University of Colorado, 3665 Discovery Drive, Boulder, CO 80303, USA

<sup>5</sup>JILA and Department of Astrophysical and Planetary Sciences, Box 440, University of Colorado, Boulder, CO 80303, USA

<sup>6</sup>Department of Astronomy, AlbaNova University Center, Stockholm University, SE-10691 Stockholm, Sweden

<sup>7</sup>Instituut-Lorentz for Theoretical Physics, Universiteit Leiden, Niels Bohrweg 2, 2333 CA Leiden, The Netherlands

<sup>8</sup>Institute of Theoretical Physics, ETH Hönggerberg, CH-8093 Zurich, Switzerland

<sup>9</sup>Discovery Center, Niels Bohr Institute, Blegdamsvej 17, DK-2100 Copenhagen, Denmark

October 1, 2018, Revision: 1.503

### ABSTRACT

Using numerical simulations, we study laminar and turbulent dynamos in chiral magnetohydrodynamics with an extended set of equations that accounts for an additional electric current due to the chiral magnetic effect (CME). This quantum relativistic phenomenon originates from an asymmetry between left- and right-handed relativistic fermions in the presence of a magnetic field and gives rise to a chiral dynamo. We show that the chiral dynamics of the magnetic field evolution proceeds in three stages: (1) a small-scale chiral dynamo instability; (2) production of chiral magnetically driven turbulence and excitation of a large-scale dynamo instability due to a new chiral  $\alpha_\mu$  effect (which is not related to kinetic helicity and becomes dominant at large fluid and magnetic Reynolds numbers); and (3) saturation of magnetic helicity and magnetic field growth controlled by a conservation law for the total chirality. The growth rate of the large-scale magnetic field and its characteristic scale measured in the numerical simulations agree well with theoretical predictions based on mean-field theory. The previously discussed two-stage chiral magnetic scenario did not include stage (2) during which the characteristic scale of magnetic field variations can increase by many orders of magnitude. Based on the findings from numerical simulations, the relevance of the CME and the revealed new chiral effects in the relativistic plasmas of the early Universe and of proto-neutron stars are discussed.

*Subject headings:* Magnetohydrodynamics – turbulence – high energy particles – magnetic fields

### 1. INTRODUCTION

Magnetic fields are observed on various spatial scales in the Universe: They are detected in planets and stars (Donati & Landstreet 2009; Reiners 2012), the interstellar medium (Crutcher 2012), and up to galactic scales (Beck 2016). Additionally, observational lower limits on intergalactic magnetic fields have been reported (Neronov & Vovk 2010; Dermer et al. 2011). Contrary to the high magnetic field strengths observed on scales below galaxy clusters, which can be explained by dynamo amplification (see, e.g., Brandenburg & Subramanian 2005), intergalactic magnetic fields, if present, are most likely of primordial origin. Due to their often large energy densities, magnetic fields play an important role in various astrophysical objects, with one prominent example being the  $\alpha\Omega$  dynamo in solar-like stars that explains stellar activity (see, e.g., Parker 1955, 1979; Moffatt 1978; Krause & Rädler 1980; Zeldovich et al. 1983; Charbonneau 2014).

While there is no doubt about the distinct role of magnetic fields in the dynamics of the present-day Universe, their origin and evolution through cosmic times remains a mystery (Rees 1987; Grasso & Rubinstein 2001; Widrow 2002; Kulsrud & Zweibel 2008). Numerous scenarios for the generation of primordial magnetic fields have been suggested in the literature. The

proposals span from inflation-produced magnetic fields (Turner & Widrow 1988) to field generation during cosmological phase transitions (Sigl et al. 1997). Even though strong magnetic fields could be generated shortly after the Big Bang, their strength subsequently decreases in cosmic expansion unless they undergo further amplification. Nevertheless, the presence of primordial magnetic fields can affect the physics of the early Universe. For example, it has been shown that primordial fields could have significant effects on the matter power spectrum, by suppression the formation of small-scale structures (Kahniashvili et al. 2013a; Pandey et al. 2015). This in turn, could influence the cosmological structure formation.

The theoretical framework for studying the evolution of magnetic fields is magnetohydrodynamics (MHD). In classical plasma physics, the system of equations includes the induction equation which is derived from the Maxwell equations and Ohm's law and describes the evolution of magnetic field, the continuity equation for the fluid density, and the Navier-Stokes equation governing the evolution of the velocity field.

At high energies, like in the quark-gluon plasma of the early Universe, however, an additional degree of freedom needs to be considered, namely the chiral chemical potential. This quantity is related to the nature of the fermionic spin which can be left-handed (spin anti-parallel to the momentum) or right-handed (spin parallel

to the momentum). An asymmetry between the number densities of left- and right-handed fermions, i.e. a nonvanishing chemical potential, leads to an additional current along magnetic field, known as the *chiral magnetic effect* (CME). This phenomenon has been discovered by Vilenkin (1980) and was later carefully investigated using different theoretical approaches in a number of studies (Redlich & Wijewardhana 1985; Tsokos 1985; Joyce & Shaposhnikov 1997; Alekseev et al. 1998; Fröhlich & Pedrini 2000, 2002; Fukushima et al. 2008; Son & Surowka 2009).

The CME causes a small-scale dynamo instability (Joyce & Shaposhnikov 1997). The evolution equation for a non-uniform chiral chemical potential has been derived by Boyarsky et al. (2012, 2015) who used it to study the inverse magnetic cascade that results in increase of the characteristic scale of the magnetic field. Boyarsky et al. (2012) have shown that the chiral asymmetry can survive down to energies of the order of 10 MeV due to coupling with an effective axion field. These studies initiated various investigations related to chiral MHD turbulence (Pavlović et al. 2017) and its role in the early Universe (Tashiro et al. 2012; Dvornikov & Semikoz 2017) as well as in neutron stars (Dvornikov & Semikoz 2015a; Sigl & Leite 2016).

Recently, a systematic theoretical analysis of the system of *chiral MHD* equations, including the back-reaction of the magnetic field on the chiral chemical potential, and the coupling to the plasma velocity field has been performed by Rogachevskii et al. (2017), referred to here as Paper I. The main findings of Paper I include a modification of MHD waves by the CME and different kinds of laminar and turbulent dynamos. Besides the well studied laminar chiral dynamo caused by the CME, a chiral-shear dynamo in the presence of a shearing velocity has been discussed there. In addition, a mean-field theory of chiral MHD in the presence of small-scale nonhelical turbulence has been developed in Paper I, where a new chiral  $\alpha_\mu$  effect that is not related to a kinetic helicity, has been found. This effect results from an interaction of the chiral magnetic fluctuations and the fluctuations of the electric current caused by the tangling magnetic fluctuations.

In the present study we perform numerical simulations, which confirm and further explore the chiral laminar and turbulent dynamos found in Paper I. To this end, we have implemented the chiral MHD equations in the PENCIL CODE<sup>1</sup>, a high-order code suitable for compressible MHD turbulence. Different situations are considered, from laminar dynamos, to chiral magnetically driven turbulence and large-scale dynamos in externally forced turbulence.

The outline of the present paper is as follows. In Section 2 we review the governing equations, the numerical setup and discuss the physics related to the two main nonlinear effects in chiral MHD, which cause different scenarios of the magnetic field evolution. In Section 3 we present numerical results on laminar chiral dynamos. In Section 4 we show how magnetic fields, amplified by the CME, produce turbulence (chiral magnetically driven turbulence). We discuss how this turbulence gives rise to the chiral  $\alpha_\mu$  effect. We also study this effect in Sec-

tion 5 for a system, where external forcing is employed to produce turbulence. After a discussion of chiral MHD in astrophysical and cosmological processes in Section 6, we draw our conclusions in Section 7.

## 2. CHIRAL MHD IN NUMERICAL SIMULATIONS

We consider a one-fluid MHD model that follows from the two-fluid model of a plasma (Artsimovich & Sagdeev 1985; Melrose 2012; Biskamp 1997).

### 2.1. Equations of chiral MHD

The system of chiral MHD equations includes the induction equation for the magnetic field  $\mathbf{B}$ , the Navier-Stokes equation for the velocity field  $\mathbf{U}$ , the continuity equation for the plasma density  $\rho$ , and the evolutionary equation for the chiral chemical potential,  $\mu = (4\alpha_{\text{em}}/\hbar c)\mu_5$ :

$$\frac{\partial \mathbf{B}}{\partial t} = \nabla \times [\mathbf{U} \times \mathbf{B} - \eta (\nabla \times \mathbf{B} - \mu \mathbf{B})], \quad (1)$$

$$\rho \frac{D\mathbf{U}}{Dt} = (\nabla \times \mathbf{B}) \times \mathbf{B} - \nabla p + \nabla \cdot (2\nu \rho \mathbf{S}) + \rho \mathbf{f}, \quad (2)$$

$$\frac{D\rho}{Dt} = -\rho \nabla \cdot \mathbf{U}, \quad (3)$$

$$\frac{D\mu}{Dt} = D_5 \Delta \mu + \lambda \eta [\mathbf{B} \cdot (\nabla \times \mathbf{B}) - \mu \mathbf{B}^2] - \Gamma_i \mu, \quad (4)$$

where the magnetic field  $\mathbf{B}$  is normalized such that the magnetic energy density is  $\mathbf{B}^2/2$  (without the  $4\pi$  factor), and  $D/Dt = \partial/\partial t + \mathbf{U} \cdot \nabla$  is the advective derivative. The chemical potential  $\mu_5 \equiv \mu_L - \mu_R$  with  $\mu_L$  and  $\mu_R$  being the chemical potentials of left- and right-chiral fermions. The chiral feedback parameter  $\lambda$  characterizes the strength of the back-reaction from the electromagnetic field on the evolution of  $\mu$ . For the case of hot plasmas (when  $k_B T \gg |\mu_L|, |\mu_R|$ ), the parameter  $\lambda$  is given by<sup>2</sup>

$$\lambda = 3\hbar c \left( \frac{8\alpha_{\text{em}}}{k_B T} \right)^2, \quad (5)$$

where  $\alpha_{\text{em}} \approx 1/137$  is the fine structure constant,  $T$  is the temperature,  $k_B$  is the Boltzmann constant,  $c$  is the speed of light, and  $\hbar$  is the reduced Planck constant. Further,  $\eta$  is the microscopic magnetic diffusivity,  $D_5$  is a chiral diffusion coefficient,  $p$  is the fluid pressure,

$$(\mathbf{S})_{ij} = \mathbf{S}_{ij} = \frac{1}{2}(U_{i,j} + U_{j,i}) - \frac{1}{3}\delta_{ij} \nabla \cdot \mathbf{U} \quad (6)$$

is the trace-free strain tensor, commas denote partial spatial differentiation,  $\nu$  is the kinematic viscosity, and  $\mathbf{f}$  is the turbulent forcing function. For an isothermal equation of state, the pressure  $p$  is related to the density  $\rho$  via  $p = c_s^2 \rho$ , where  $c_s$  is the sound speed.

In analogy with mean-field dynamo theory, where a large-scale magnetic field is amplified by the  $\alpha$  effect leading to an  $\alpha^2$  dynamo, we use in the present study the name  $v_\mu^2$  dynamo, where

$$v_\mu \equiv \eta \mu_0 \quad (7)$$

plays the role of  $\alpha$ , see Equation (1), and  $\mu_0$  is the initial value of the chemical potential  $\mu$ . These different

<sup>1</sup> <http://pencil-code.nordita.org/>

<sup>2</sup> The definition of  $\lambda$  in the case of a degenerate Fermi gas will be given in Section 6.2.

notions are caused by the fact that the  $v_\mu$  effect is not related to the turbulence effect, i.e., it is not determined by the mean electromotive force, but is originated from the CME (see for details Paper I). The  $\Gamma_f$  term in Equation (4) describes the chirality flipping processes due to finite fermion mass. It is neglected here due to the dominance of the remaining terms.

In Equations (1) and (4),  $\mu$  has the dimension of inverse length, and  $\lambda^{-1}$  has the dimension of energy per unit length. We will use this system of chiral MHD equations to study in numerical simulations various laminar and turbulent dynamos as well as a production of turbulence by the CME. Equations (1)–(4) are written for the case of small magnetic diffusivity, typical for astrophysical systems with large magnetic Reynolds numbers; see Paper I.

The system of Equations (1)–(4) obeys a conservation law:

$$\frac{\partial}{\partial t} \left( \frac{\lambda}{2} \mathbf{A} \cdot \mathbf{B} + \mu \right) + \nabla \cdot \mathbf{F}_{\text{tot}} = 0, \quad (8)$$

where

$$\mathbf{F}_{\text{tot}} = \frac{\lambda}{2} (\mathbf{E} \times \mathbf{A} + \mathbf{B} \Phi) - D_5 \nabla \mu \quad (9)$$

is the flux of total chirality and  $\mathbf{B} = \nabla \times \mathbf{A}$ , with  $\mathbf{A}$  being the vector potential,  $\mathbf{E} = -c^{-1} \{ \mathbf{U} \times \mathbf{B} + \eta (\mu \mathbf{B} - \nabla \times \mathbf{B}) \}$  is the electric field,  $\Phi$  is the electrostatic potential, and  $\lambda$  is assumed constant. This implies that the total chirality, is a conserved quantity:

$$\frac{\lambda}{2} \langle \mathbf{A} \cdot \mathbf{B} \rangle + \bar{\mu} = \mu_0 = \text{const}, \quad (10)$$

where  $\bar{\mu}$  is spatially averaged value of the chemical potential and  $\langle \mathbf{A} \cdot \mathbf{B} \rangle$  is the magnetic helicity.

### 2.2. Chiral MHD equations in dimensionless form

The system of Equations (1)–(4) can be written in non-dimensional form, where velocity is measured in units of the sound speed  $c_s$ , length is measured in units of  $\ell_\mu \equiv \mu_0^{-1}$ , so time is measured in units of  $\ell_\mu/c_s$ , the magnetic field is measured in units of  $\sqrt{\bar{\rho}} c_s$ , fluid density is measured in units of  $\bar{\rho}$  and the chiral chemical potential is measured in units of  $\ell_\mu^{-1}$ , where  $\bar{\rho}$  is the volume-averaged density. Thus, we introduce the following dimensionless functions, indicated by a tilde:  $\mathbf{B} = \sqrt{\bar{\rho}} c_s \tilde{\mathbf{B}}$ ,  $\mathbf{U} = c_s \tilde{\mathbf{U}}$ ,  $\mu = \ell_\mu^{-1} \tilde{\mu}$  and  $\rho = \bar{\rho} \tilde{\rho}$ . The chiral MHD equations in non-dimensional form are given by

$$\frac{\partial \tilde{\mathbf{B}}}{\partial \tilde{t}} = \tilde{\nabla} \times \left[ \tilde{\mathbf{U}} \times \tilde{\mathbf{B}} + \text{Ma}_\mu (\tilde{\mu} \tilde{\mathbf{B}} - \tilde{\nabla} \times \tilde{\mathbf{B}}) \right], \quad (11)$$

$$\tilde{\rho} \frac{D \tilde{\mathbf{U}}}{D \tilde{t}} = (\tilde{\nabla} \times \tilde{\mathbf{B}}) \times \tilde{\mathbf{B}} - \tilde{\nabla} \tilde{\rho} + \text{Re}_\mu^{-1} \tilde{\nabla} \cdot (2\nu \tilde{\rho} \tilde{\mathbf{S}}) + \tilde{\rho} \tilde{\mathbf{f}}, \quad (12)$$

$$\frac{D \tilde{\rho}}{D \tilde{t}} = -\tilde{\rho} \nabla \cdot \tilde{\mathbf{U}}, \quad (13)$$

$$\frac{D \tilde{\mu}}{D \tilde{t}} = D_\mu \tilde{\Delta} \tilde{\mu} + \Lambda_\mu \left[ \tilde{\mathbf{B}} \cdot (\tilde{\nabla} \times \tilde{\mathbf{B}}) - \tilde{\mu} \tilde{\mathbf{B}}^2 \right], \quad (14)$$

where we introduce the following non-dimensional parameters:

- the chiral Mach number:

$$\text{Ma}_\mu = \frac{\eta \mu_0}{c_s} \equiv \frac{v_\mu}{c_s}, \quad (15)$$

- the magnetic Prandtl number:

$$\text{Pr}_M = \frac{\nu}{\eta}, \quad (16)$$

- the chiral Prandtl number:

$$\text{Pr}_\mu = \frac{\nu}{D_5}, \quad (17)$$

- the chiral nonlinearity parameter:

$$\lambda_\mu = \lambda \eta^2 \bar{\rho}, \quad (18)$$

so that  $D_\mu = \text{Ma}_\mu \text{Pr}_M / \text{Pr}_\mu$ ,  $\Lambda_\mu = \lambda_\mu / D_\mu$  and  $\text{Re}_\mu = (\text{Ma}_\mu \text{Pr}_M)^{-1}$ .

### 2.3. Physics of different regimes of magnetic field evolution

There are two main nonlinear effects which determine the dynamics of the magnetic field in chiral MHD. The first nonlinear effect is determined by the conservation law (8) for the total chirality which follows from the induction equation and the equation for the chiral magnetic potential. The second nonlinear effect is determined by the Lorentz force in the Navier-Stokes equation.

If the magnetic field evolution starts from a very small force-free magnetic field, the second nonlinear effect due to the Lorentz force vanishes if we assume that the magnetic field remains force-free. The magnetic field is generated by the chiral magnetic dynamo instability with a maximum growth rate  $\gamma_\mu^{\text{max}} = v_\mu^2 / 4\eta$  attained at the wavenumber  $k_\mu = \mu_0 / 2$  (Joyce & Shaposhnikov 1997).

Since the total chirality is conserved, the increase of the magnetic field in the nonlinear stage results in a decrease of the chiral chemical potential, so that the characteristic scale at which the growth rate is maximum, increases in time. This nonlinear effect has been interpreted in terms of an inverse magnetic cascade (Boyarsky et al. 2012). The maximum saturated level of the magnetic field can be estimated from the conservation law (8):  $B_{\text{sat}} \sim (\mu_0 k_M / \lambda)^{1/2} < \mu_0 / \lambda^{1/2}$ . Here  $\mu_{\text{sat}} \ll \mu_0$  is the chiral chemical potential at saturation with  $k_M < \mu_0$  is the characteristic wavenumber, which corresponds to the maximum of the magnetic energy.

However, the growing force-free magnetic field cannot stay force-free in the nonlinear stage of the magnetic field evolution. If the Lorentz force does not vanish, it generates small-scale velocity fluctuations. This nonlinear stage begins when the nonlinear term  $\mathbf{U} \times \mathbf{B}$  in Equation (1) is of the order of the dynamo generating term  $v_\mu \mathbf{B}$ , i.e., when the velocity reaches the level of  $U \sim v_\mu$ . The described effect results in the production of chiral magnetically driven turbulence with the level of turbulent kinetic energy being determined by the balance of the nonlinear term  $(\mathbf{U} \cdot \nabla) \mathbf{U}$  in Equation (2) and the Lorentz force  $(\nabla \times \mathbf{B}) \times \mathbf{B}$ , so that the turbulent velocity can reach the Alfvén speed  $v_A = (\mathbf{B}^2 / \bar{\rho})^{1/2}$ .

The chiral magnetically driven turbulence causes complicated dynamics: the magnetic diffusion increases

by turbulence and the produced mean electromotive force and the chiral  $\alpha_\mu$  effect generate large-scale magnetic fields; see Paper I. The generated large-scale magnetic fields are concentrated at the wavenumber  $k_\alpha = k_\mu(2 \ln \text{Re}_M)/(3\text{Re}_M)$  for  $\text{Re}_M \gg 1$  (see Paper I), and the saturated value of the large-scale magnetic field controlled by the conservation law (8), is  $B_{\text{sat}} \sim (\mu_0 k_\alpha / \lambda)^{1/2}$ . Here  $\text{Re}_M$  is the magnetic Reynolds number based on the integral scale of turbulence and the turbulent velocity at this scale.

Depending on the chiral nonlinearity parameter  $\lambda_\mu$ , there are two or three stages of magnetic field evolution. In particular, when  $\lambda_\mu$  is very small, there is sufficient time to produce turbulence and excite the large-scale dynamo, so that the magnetic field evolution includes three stages:

- (1) the small-scale chiral dynamo instability,
- (2) the production of chiral magnetically driven MHD turbulence and the excitation of a large-scale dynamo instability, and
- (3) the saturation of magnetic helicity and magnetic field growth controlled by the conservation law (8).

If  $\lambda_\mu$  is not very small, so that the saturated value of the magnetic field is not large, there is not enough time to excite the large-scale dynamo instability. In this case, the magnetic field dynamics includes two stages:

- (1) the chiral dynamo instability,
- (2) the saturation of magnetic helicity and magnetic field growth controlled by the conservation law (8) for the total chirality.

#### 2.4. Characteristic scales of chiral magnetically driven turbulence

In the nonlinear regime, once turbulence is fully developed, small-scale magnetic fields can be excited over a broad range of wavenumbers up to the diffusion cutoff wavenumber. Using dimensional arguments and numerical simulations, [Brandenburg et al. \(2017b\)](#) found that for chiral magnetically driven turbulence, the magnetic energy spectrum  $E_M(k, t)$  obeys

$$E_M(k, t) = C_\mu \bar{\rho} \mu_0^3 \eta^2 k^{-2}, \quad (19)$$

where  $C_\mu \approx 16$  is a chiral magnetic Kolmogorov-type constant. Here,  $E_M(k, t)$  is normalized such that  $\mathcal{E}_M = \int E_M(k) dk = \langle \mathbf{B}^2 \rangle / 2$  is the mean magnetic energy density. It was also confirmed numerically by [Brandenburg et al. \(2017b\)](#) that the magnetic energy spectrum  $E_M(k)$  is limited from above by  $C_\lambda \mu_0 / \lambda$ , where  $C_\lambda \approx 1$  is another empirical constant. This yields a critical minimum wavenumber,

$$k_\lambda = \sqrt{\bar{\rho} \lambda \frac{C_\mu}{C_\lambda} \mu_0 \eta}, \quad (20)$$

below which the spectrum will no longer be proportional to  $k^{-2}$ .

The spectrum extends to larger wavenumbers up to a diffusive cutoff wavenumber  $k_{\text{diff}}$ . The diffusion scale for a magnetically produced turbulence is determined by the condition  $\text{Lu}(k_{\text{diff}}) = 1$ , where  $\text{Lu}(k) = v_A(k) / \eta k$  is the scale-dependent Lundquist number,  $v_A(k) = (\langle \mathbf{B}^2 \rangle_k / \bar{\rho})^{1/2}$  is the scale-dependent Alfvén speed and  $\langle \mathbf{B}^2 \rangle_k = 2 \int_{k_\lambda}^k E_M(k) dk$ . To determine the Alfvén speed,

TABLE 1  
OVERVIEW OF RUNS FOR THE LAMINAR  $v_\mu^2$  DYNAMOS.

simulation	$\text{Pr}_M$	$\lambda_\mu$	$\frac{\text{Ma}_\mu}{10^{-3}}$	$\frac{k_\lambda}{10^{-4} \mu_0}$	$\frac{k_{\text{diff}}}{\mu_0}$
La2-1B	1.0	$1 \times 10^{-8}$	2	4.0	283
La2-2B	0.5	$4 \times 10^{-8}$	4	8.0	200
La2-3B	0.2	$2.5 \times 10^{-7}$	10	20	126
La2-4B	2.0	$2.5 \times 10^{-9}$	1	2.0	400
La2-5B	1.0	$1 \times 10^{-9}$	1.5	1.3	503
La2-5G	1.0	$1 \times 10^{-8}$	1.5	4.0	283
La2-6G	1.0	$1 \times 10^{-5}$	2	130	50
La2-7B	1.0	$1 \times 10^{-9}$	3	4.0	283
La2-7G	1.0	$1 \times 10^{-9}$	3	4.0	283
La2-8B	1.0	$1 \times 10^{-9}$	5	4.0	283
La2-8G	1.0	$1 \times 10^{-9}$	5	4.0	283
La2-9B	1.0	$1 \times 10^{-9}$	10	4.0	283
La2-9G	1.0	$1 \times 10^{-9}$	10	4.0	283
La2-10B	1.0	$1 \times 10^{-5}$	20	130	50
La2-10Bkmax	1.0	$1 \times 10^{-5}$	20	130	50
La2-10G	1.0	$1 \times 10^{-5}$	20	4.0	283
La2-11B	1.0	$1 \times 10^{-9}$	50	1.3	503
La2-11G	1.0	$1 \times 10^{-8}$	50	4.0	283
La2-12B	1.0	$1 \times 10^{-9}$	2	1.3	503
La2-13B	1.0	$1 \times 10^{-7}$	2	13	159
La2-14B	1.0	$3 \times 10^{-9}$	2	2.2	382
<b>La2-15B</b>	<b>1.0</b>	<b><math>1 \times 10^{-5}</math></b>	<b>2</b>	<b>130</b>	<b>50</b>
La2-16B	1.0	$3 \times 10^{-8}$	2	6.9	215

$v_A(k)$ , we integrate Equation (19) over  $k$  and obtain

$$v_A(k) = \eta \mu_0 \left( \frac{2 C_\mu \mu_0}{k_\lambda} \right)^{1/2} \left( 1 - \frac{k_\lambda}{k} \right)^{1/2}. \quad (21)$$

The conditions  $\text{Lu}(k_{\text{diff}}) = 1$  and  $k_{\text{diff}} \gg k_\lambda$  yield

$$k_{\text{diff}} = \sqrt{2} \left( \frac{C_\mu C_\lambda}{\lambda_\mu} \right)^{1/4} \mu_0 \approx 2.8 \lambda_\mu^{-1/4} \mu_0. \quad (22)$$

Numerical simulations by [Brandenburg et al. \(2017b\)](#) have been performed for  $0.75 \leq k_{\text{diff}} / \mu_0 \leq 75$ . In the present DNS, we use values in the range from 4.5 to 503.

#### 2.5. DNS with the PENCIL CODE

We solve Equations (11)–(14) numerically using the PENCIL CODE. This code uses sixth-order explicit finite differences in space and a third-order accurate time-stepping method ([Brandenburg & Dobler 2002](#); [Brandenburg 2003](#)). The boundary conditions are periodic in all three directions. All simulations presented in Sections 3 and 4 are performed without external forcing of turbulence. In Section 5 we apply a turbulent forcing function  $\mathbf{f}$  in the Navier-Stokes equation which consists of random plane transverse white-in-time, unpolarized waves. Hereafter, when we discuss numerical simulations, all quantities are considered as nondimensional quantities and we drop the tildes from now on for simplicity. The wavenumber  $k_1 = 2\pi/L$  is based on the size of the box  $L = 2\pi$ . In all runs, we set  $k_1 = 1$ ,  $c_s = 1$  and the mean fluid density  $\bar{\rho} = 1$ .

### 3. LAMINAR CHIRAL DYNAMOS

In this section we study numerically laminar chiral dynamos in the absence of any turbulence (externally or chiral magnetically driven).



### 3.1. Numerical setup

Parameters and initial conditions for all laminar dynamo simulations are listed in Tables 1 and 2. All of these simulations are two-dimensional and have a resolution of  $256^2$ . Runs with names ending with ‘B’ are with the initial conditions for the magnetic field in the form of a Beltrami magnetic field:  $B(t=0) = 10^{-4}(0, \sin x, \cos x)$ , while runs with names ending with ‘G’ are initiated with Gaussian noise. The initial conditions for the velocity field for the laminar  $v_\mu^2$  dynamo are  $U(t=0) = (0, 0, 0)$ , and for the laminar chiral–shear dynamos (the  $v_\mu^2$ –shear or  $v_\mu$ –shear dynamos) are  $U(t=0) = (0, S_0 \cos x, 0)$  with the non-dimensional shear rate  $S_0$  given for all runs.

We set  $\text{Pr}_\mu = 1$  for the chiral Prandtl number in all runs. In many runs the magnetic Prandtl number  $\text{Pr}_M = 1$  (except for several runs for the laminar  $v_\mu^2$  dynamo, see Table 1). The reference runs for the laminar  $v_\mu^2$  dynamo (La2-15B) and the chiral–shear dynamos (LaU-4G) are shown in bold in Tables 1 and 2. The results of numerical simulations are compared with theoretical predictions.

### 3.2. Laminar $v_\mu^2$ dynamo

We start with the situation without an imposed fluid flow where the chiral laminar  $v_\mu^2$  dynamo can be excited.

#### 3.2.1. Theoretical aspects

In this section, we outline the theoretical predictions for laminar chiral dynamo (for details see Paper I). To determine the chiral dynamo growth rate, we seek a solution of the linearized Equation (1) for small perturbations of the following form:  $\mathbf{B}(t, x, z) = B_y(t, x, z)\mathbf{e}_y + \nabla \times [A(t, x, z)\mathbf{e}_y]$ , where  $\mathbf{e}_y$  is the unit vector in the  $y$ -direction.

We consider the equilibrium configuration:  $\mu = \mu_0 = \text{const}$  and  $\mathbf{U}_0 = 0$ . The functions  $B_y(t, x, z)$  and  $A(t, x, z)$  are determined by the equations

$$\frac{\partial A(t, x, z)}{\partial t} = v_\mu B_y + \eta \Delta A, \quad (23)$$

$$\frac{\partial B_y(t, x, z)}{\partial t} = -v_\mu \Delta A + \eta \Delta B_y, \quad (24)$$

where  $v_\mu = \eta \mu_0$ ,  $\Delta = \nabla_x^2 + \nabla_z^2$ , and the remaining components of the magnetic field are given by  $B_x = -\nabla_z A$  and  $B_z = \nabla_x A$ . We seek a solution to Equations (23) and (24) of the form  $A, B_y \propto \exp[\gamma t + i(k_x x + k_z z)]$ . The growth rate of the dynamo instability is given by:

$$\gamma = |v_\mu k| - \eta k^2, \quad (25)$$

where  $k^2 = k_x^2 + k_z^2$ . The dynamo instability is excited (i.e.,  $\gamma > 0$ ) for  $k < |\mu_0|$ . The maximum growth rate of the dynamo instability,

$$\gamma_\mu^{\text{max}} = \frac{v_\mu^2}{4\eta}, \quad (26)$$

is attained at

$$k_\mu = \frac{1}{2}|\mu_0|. \quad (27)$$

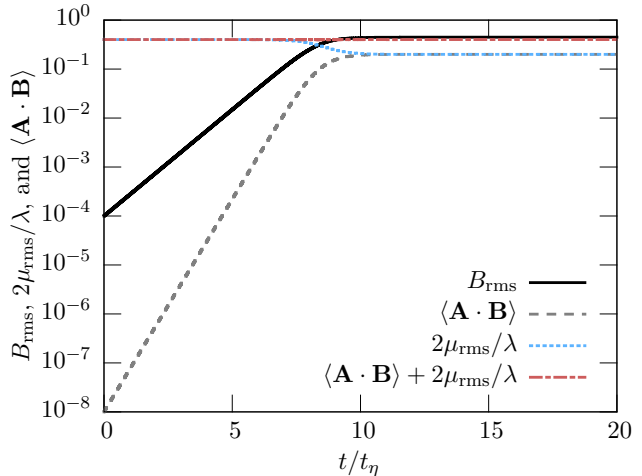


FIG. 1.— **Laminar  $v_\mu^2$  dynamo:** Time evolution of  $B_{\text{rms}}$  (solid black line),  $\langle \mathbf{A} \cdot \mathbf{B} \rangle$  (dashed gray line),  $\mu_{\text{rms}}$  (multiplied by  $2/\lambda$ , dotted blue line), and  $\langle \mathbf{A} \cdot \mathbf{B} \rangle + 2\mu_{\text{rms}}/\lambda$  (dashed-dotted red line) for reference run La2-15B (see table 1).

#### 3.2.2. Time evolution

In Figure 1 we show the time evolution of the rms magnetic field  $B_{\text{rms}}$ , the magnetic helicity  $\langle \mathbf{A} \cdot \mathbf{B} \rangle$ , the chemical potential  $\mu_{\text{rms}}$  (multiplied by a factor of  $2/\lambda$ ), and  $\langle \mathbf{A} \cdot \mathbf{B} \rangle + 2\mu_{\text{rms}}/\lambda$  for reference run La2-15B. In simulations the time is measured in units of diffusion time  $t_\eta = (\eta k_1^2)^{-1}$ . The initial conditions for the magnetic field are chosen in the form of a Beltrami field on  $k = k_1 = 1$ .

The magnetic field is amplified exponentially over more than four orders of magnitude until it saturates at roughly eight diffusive times. Within the same time the magnetic helicity  $\langle \mathbf{A} \cdot \mathbf{B} \rangle$  increases over more than eight orders of magnitude. Since the sum of magnetic helicity and  $2\mu/\lambda$  is conserved, the chemical potential  $\mu$  decreases in a nonlinear stage of the evolution from the initial value  $\mu_0 = 2$  to  $\mu = 1$ , resulting in a saturation of the laminar  $v_\mu^2$  dynamo.

#### 3.2.3. Dynamo growth rate

In Figure 2, we show the growth rate as a function of the chiral Mach number,  $\text{Ma}_\mu$ . The black solid line in this figure shows the theoretical prediction for the maximum growth rate  $\gamma_\mu^{\text{max}}$  that is attained at  $k_\mu = \mu_0/2 = 1$ ; see Equations (26) and (27). When the initial magnetic field is distributed over all spatial scales, like in the case of initial magnetic Gaussian noise, i.e., there is a nonvanishing magnetic field at  $k_\mu$ ; that is inside the computational domain, the initial magnetic field is excited with the maximum growth rate as observed in the simulations. Consequently, the runs with Gaussian initial fields shown as red diamonds in Figure 2, lie on the theoretical curve  $\gamma_\mu^{\text{max}}$ . The dotted line in Figure 2 corresponds to the theoretical prediction for the growth rate  $\gamma$  at the scale of the box ( $k = 1$ ). The excitation of the magnetic field from an initial Beltrami field on  $k = 1$  occurs with the growth rates in agreement with the theoretical dotted curve (see blue diamonds in Figure 2).

#### 3.2.4. Dependence on the initial conditions

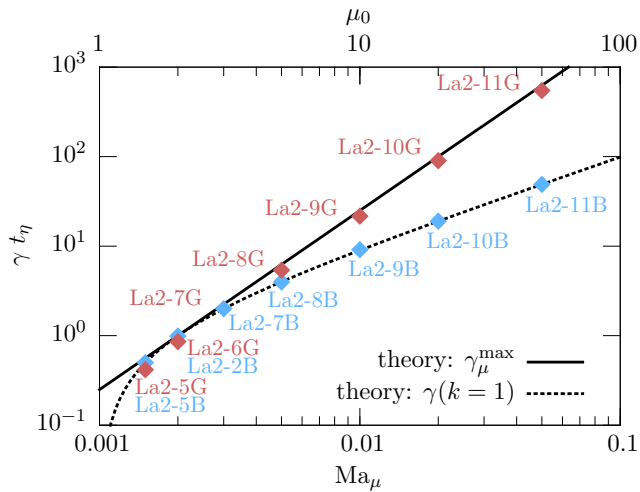


FIG. 2.— **Laminar  $v_\mu^2$  dynamo:** Growth rates as a function of  $Ma_\mu$ , for simulations with  $\mu_0 = 2$ . The black line is the theoretical prediction for the maximum growth rate  $\gamma_\mu^{\max}$  (see Equation 26) that is attained at  $k_\mu = \mu_0/2 = 1$ ; (see Equation 27). The runs with Gaussian initial fields shown as red diamonds, lie on the theoretically predicted  $\gamma_\mu^{\max}$ . The dotted line corresponds to the theoretical prediction for the growth rate  $\gamma(k=1)$  at the scale of the box. The runs with an initial magnetic Beltrami field on  $k=1$  shown as blue diamonds, lie on the theoretically predicted dotted curve  $\gamma(k=1)$ .

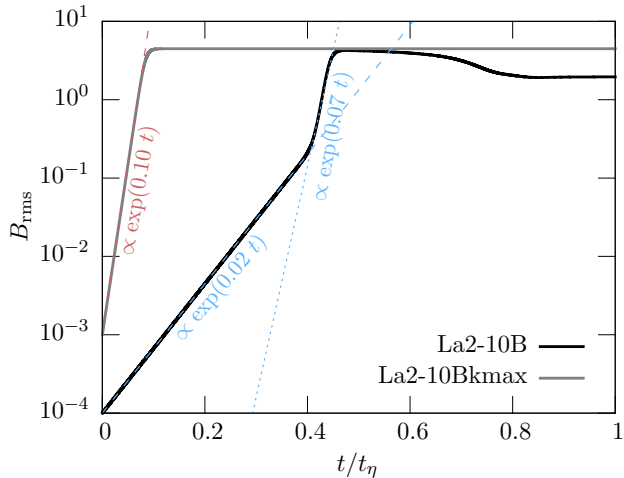


FIG. 3.— **Laminar  $v_\mu^2$  dynamo:** Time evolution of  $B_{rms}$  for two different initial conditions. The black line is for the dynamo instability started from an initial Beltrami field at  $k=1$  (run La2-10B), while the blue line is for an initial Beltrami field with  $k=10$  (run La2-10Bkmax). Fits in different regimes are indicated by thin lines. Both runs are for the initial value  $\mu_0 = 20$ , so that  $k_\mu = 10$ ; and  $\gamma_\mu^{\max} = 0.1$  (see Equation 26).

The initial conditions for the magnetic field are important mostly at early times. If the magnetic field is initially concentrated on the box scale, we expect to observe a growth rate  $\gamma(k=1)$  as given by Equation (25). At later times, the spectrum of the magnetic field can, however, be changed due to mode coupling, and be amplified with a larger growth rate. This behavior is observed in Figure 3, where an initial Beltrami field with  $k=10$  is excited with the maximum growth rate, since  $\mu_0 = 20$ . In Figure 3 we also consider another situation

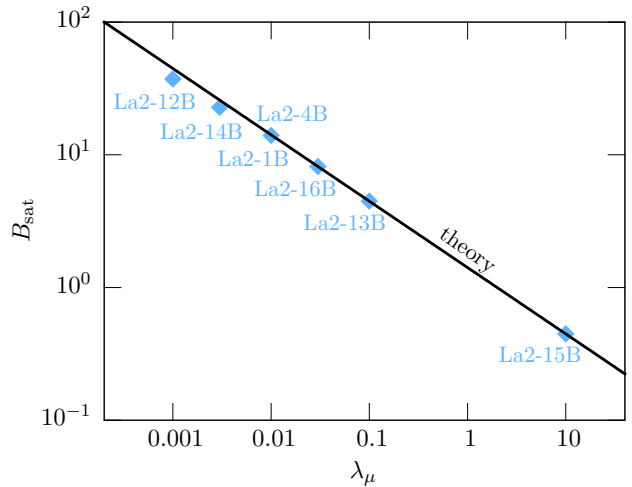


FIG. 4.— **Laminar  $v_\mu^2$  dynamo:** The saturation magnetic field strength for simulations with different  $\lambda_\mu$ . Details for the different runs, given by labeled blue diamonds, can be found in Table 1.

where the dynamo is started from an initial Beltrami field with  $k=1$  (La2-10B). In this case, the dynamo started with the growth rate  $\gamma = 0.019$ , which is consistent with the theoretical prediction for  $\gamma(k=1)$ . Later, after approximately  $0.01 \tau_\eta$ , the dynamo growth rate increases up to the value  $\gamma = 0.07$ , which is close to the maximum growth rate  $\gamma_\mu^{\max} = 0.1$ .

### 3.2.5. Saturation

The parameter  $\lambda$  in the evolution Equation (4), or the corresponding dimensionless parameter  $\lambda_\mu$  in Equation (14), for the chemical potential determines the non-linear saturation of the chiral dynamo. We determine the saturation value of the magnetic field  $B_{sat}$  numerically for different values of  $\lambda_\mu$  (see Figure 4). We find that the saturation value of the magnetic field increases with decreasing  $\lambda_\mu$ . This can be expected from the conservation law (8). If the initial magnetic energy is very small, we find from Equation (8) the following estimate for the saturated magnetic field during laminar chiral dynamo action:

$$B_{sat} \sim \left[ \frac{\mu_0(\mu_0 - \mu_{sat})}{\lambda} \right]^{1/2}, \quad (28)$$

where  $\mu_{sat}$  is the chiral chemical potential at saturation and we use the estimate for  $A \approx 2B/\mu_0$ . Inspection of Figure 4 demonstrates a good agreement between theoretical (solid line) and numerical results (blue diamonds).

## 3.3. Laminar chiral-shear dynamos

In this section we consider laminar chiral dynamos in the presence of an imposed shearing velocity. Such non-uniform velocity profile can be created in different astrophysical flows.

### 3.3.1. Theoretical aspects

Here we outline the theoretical predictions for laminar chiral dynamos in the presence of an imposed shearing velocity (for details see Paper I). We consider the equilibrium configuration specified by the shear velocity

$U_{\text{eq}} = (0, Sx, 0)$ , and  $\mu = \mu_0 = \text{const.}$  This implies that the fluid has non-zero vorticity  $\mathbf{W} = (0, 0, S)$  similar to differential (non-uniform) rotation. The functions  $B_y(t, x, z)$  and  $A(t, x, z)$  are determined by

$$\frac{\partial A(t, x, z)}{\partial t} = v_\mu B_y + \eta \Delta A, \quad (29)$$

$$\frac{\partial B_y(t, x, z)}{\partial t} = -S \nabla_z A - v_\mu \Delta A + \eta \Delta B_y. \quad (30)$$

We look for a solution to Equations (29) and (30) of the form  $A, B_y \propto \exp[\gamma t + i(k_x x + k_z z - \omega t)]$ . The growth rate of the dynamo instability and the frequency of the dynamo waves are:

$$\gamma = \frac{|v_\mu k|}{\sqrt{2}} \left\{ 1 + \left[ 1 + \left( \frac{S k_z}{v_\mu k^2} \right)^2 \right]^{\frac{1}{2}} \right\}^{\frac{1}{2}} - \eta k^2, \quad (31)$$

$$\omega = \text{sgn}(\mu_0 k_z) \frac{S k_z}{\sqrt{2} k} \left\{ 1 + \left[ 1 + \left( \frac{S k_z}{v_\mu k^2} \right)^2 \right]^{\frac{1}{2}} \right\}^{-\frac{1}{2}}. \quad (32)$$

This solution describes a laminar  $v_\mu^2$ -shear dynamo for arbitrary values of the shear rate  $S$ .

Next, we consider a situation where the shear term on the right side of Equation (30) dominates, i.e., where  $|S \nabla_z A| \gg |v_\mu \Delta A|$ . Thus, the growth rate of the dynamo instability and the frequency of the dynamo waves are:

$$\gamma = \left( \frac{|v_\mu S k_z|}{2} \right)^{1/2} - \eta k^2, \quad (33)$$

$$\omega = \text{sgn}(\mu_0 k_z) \left( \frac{|v_\mu S k_z|}{2} \right)^{1/2}. \quad (34)$$

The dynamo is excited for  $k < |v_\mu S k_z / 2 \eta^2|^{1/4}$ . The maximum growth rate of the dynamo instability and the frequency  $\omega = \omega(k = k_z^\mu)$  of the dynamo waves are attained at

$$k_z^\mu = \frac{1}{4} \left( \frac{2 |S v_\mu|}{\eta^2} \right)^{1/3}, \quad (35)$$

and are given by

$$\gamma_\mu^{\text{max}} = \frac{3}{8} \left( \frac{S^2 v_\mu^2}{2 \eta} \right)^{1/3} - \eta k_x^2, \quad (36)$$

$$\omega(k = k_z^\mu) = \frac{\text{sgn}(v_\mu k_z)}{2 \eta} \left( \frac{S^2 v_\mu^2}{2 \eta} \right)^{1/3}. \quad (37)$$

This solution describes the laminar  $v_\mu$ -shear dynamo.

### 3.3.2. Simulations of laminar $v_\mu$ -shear dynamo

Since our simulations have periodic boundary conditions, we model shear velocities as  $U_S = (0, u_S \cos x, 0)$ . The mean shear velocity  $\bar{u}_S$  over half the box is  $\bar{u}_S = (2/\pi) u_S$ . In Figure 5 we show the time evolution of the magnetic field (which starts to be excited from a Gaussian initial field), the velocity  $u_{\text{rms}}$ , the magnetic helicity  $\langle \mathbf{A} \cdot \mathbf{B} \rangle$ , the chemical potential  $\mu_{\text{rms}}$  (multiplied by a factor of  $2/\lambda$ ), and  $\langle \mathbf{A} \cdot \mathbf{B} \rangle + 2\mu_{\text{rms}}/\lambda$  for run LaU-4G.

TABLE 2  
OVERVIEW OF RUNS FOR THE CHIRAL-SHEAR DYNAMOS.

simulation	$\lambda_\mu$	$\frac{\text{Ma}_\mu}{10^{-3}}$	$u_S$	$\frac{k_\lambda}{10^{-4} \mu_0}$	$\frac{k_{\text{diff}}}{\mu_0}$
LaU-1B	$1 \times 10^{-9}$	2.0	0.01	1.3	503
LaU-1G	$1 \times 10^{-9}$	2.0	0.01	1.3	503
LaU-2B	$1 \times 10^{-9}$	2.0	0.02	1.3	503
LaU-2G	$1 \times 10^{-9}$	2.0	0.02	1.3	503
LaU-3B	$1 \times 10^{-9}$	2.0	0.05	1.3	503
LaU-3G	$1 \times 10^{-9}$	2.0	0.05	1.3	503
LaU-4B	$1 \times 10^{-9}$	2.0	0.10	1.3	503
<b>LaU-4G</b>	<b><math>1 \times 10^{-5}</math></b>	<b>2.0</b>	<b>0.10</b>	<b>126</b>	<b>50</b>
LaU-5B	$1 \times 10^{-9}$	2.0	0.20	1.3	503
LaU-5G	$1 \times 10^{-9}$	2.0	0.20	1.3	503
LaU-6B	$1 \times 10^{-9}$	2.0	0.50	1.3	503
LaU-6G	$1 \times 10^{-9}$	2.0	0.50	1.3	503
LaU-7G	$1 \times 10^{-8}$	10	0.01	4.0	283
LaU-8G	$1 \times 10^{-8}$	10	0.05	4.0	283
LaU-9G	$1 \times 10^{-8}$	10	0.10	4.0	283
LaU-10G	$1 \times 10^{-8}$	10	0.50	4.0	283

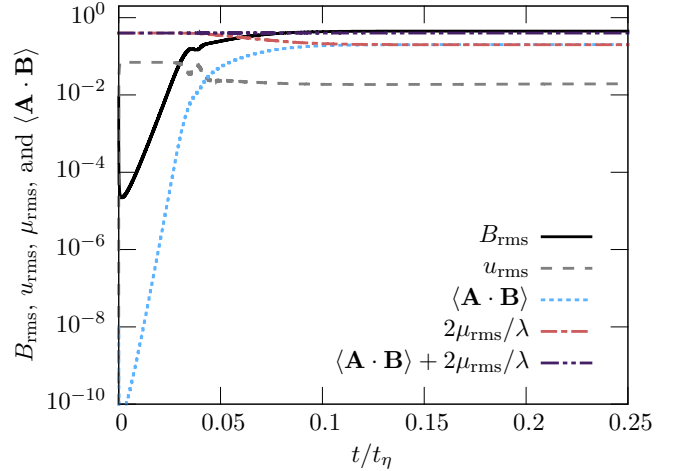


FIG. 5.— **Laminar  $v_\mu$ -shear dynamo:** Time evolution of the magnetic field  $B_{\text{rms}}$ , the velocity  $u_{\text{rms}}$ , the magnetic helicity  $\langle \mathbf{A} \cdot \mathbf{B} \rangle$ , the chemical potential  $\mu_{\text{rms}}$  (multiplied by a factor of  $2/\lambda$ ), and  $\langle \mathbf{A} \cdot \mathbf{B} \rangle + 2\mu_{\text{rms}}/\lambda$  (run LaU-4G).

The growth rate for the chiral-shear dynamo (the  $v_\mu^2$ -shear dynamo) is larger than that for the laminar chiral dynamo (the  $v_\mu^2$ -dynamo). After a time of roughly  $0.03 t_\eta$ , the system enters the nonlinear phase, in which the velocity field is affected by the magnetic field, but the magnetic field can still slowly increase. Saturation of the dynamo occurs after approximately  $0.1 t_\eta$ .

For Gaussian initial fields, we have observed a short delay in the growth of the magnetic field. In both cases, the dynamo growth rate increases with increasing shear. As in the case of the chiral  $v_\mu^2$  dynamo, we observe perfect conservation of the quantity  $\langle \mathbf{A} \cdot \mathbf{B} \rangle + 2\mu_{\text{rms}}/\lambda$  in the simulations of the laminar  $v_\mu$ -shear dynamo.

In Figure 6 we show the theoretical dependence of the growth rate  $\gamma$  and the dynamo frequency  $\omega$  on the shear velocity  $\bar{u}_S$  for Beltrami initial conditions at different wavenumbers; see Equations (33) and (36). The blue diamonds correspond to the numerical results. Within

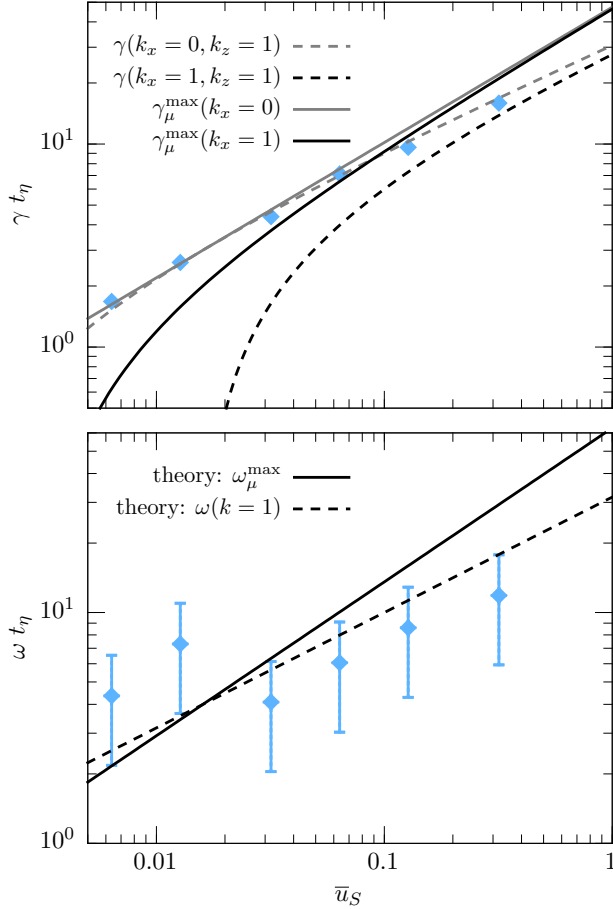


FIG. 6.— **Laminar  $v_\mu$ -shear dynamo:** Growth rate (top panel) and dynamo frequency (bottom panel) as a function of the mean shear  $\bar{u}_S$  for the Beltrami initial field (runs LaU- $n$ B with  $n = 1 - 6$ , see Table 2).

the error bars, the theoretical and numerical results are in agreement.

### 3.3.3. Simulations of the laminar $v_\mu^2$ -shear dynamo

The growth rate of chiral-shear dynamos versus mean shear in the range between  $u_S = 0.01$  and  $0.5$  is shown in Figure 7. We choose a large initial value of the chemical potential, i.e.  $\mu_0 = 10$ , to ensure that  $k_{\max}$  is within the box for all values of  $\bar{u}_S$ . We overplot the growth rates found from the simulations with the maximum growth rate given by Equation (31). In addition, we show the theoretical predictions for the limiting cases of the  $v_\mu^2$  and  $v_\mu$ -shear dynamos; see Equations (26) and (36). Inspection of Figure 7 shows that the results obtained from the simulations agree with theoretical predictions.

## 4. CHIRAL MAGNETICALLY DRIVEN TURBULENCE

In this section we will show that the CME can drive turbulence via the Lorentz force in the Navier-Stokes equation. When the magnetic field increases exponentially due to the small-scale chiral magnetic dynamo with growth rate  $\gamma$ , the Lorentz force,  $(\nabla \times \mathbf{B}) \times \mathbf{B}$ , increases at the rate  $2\gamma$ . The laminar dynamo occurs only up to the first nonlinear phase, when the Lorentz force starts to produce turbulence (referred as a chiral magnetically

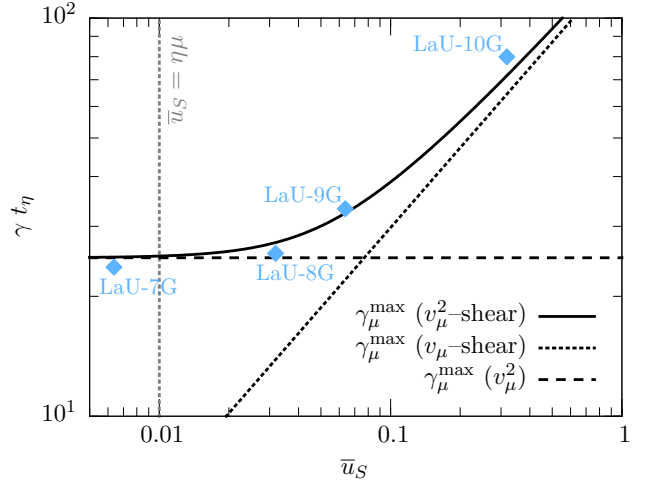


FIG. 7.— **Laminar  $v_\mu^2$ -shear dynamo:** Growth rate  $\gamma$  as a function of mean shear  $\bar{u}_S$ . For comparison we plot the maximum growth rate of  $v_\mu^2$  dynamo (26) and of the  $v_\mu$ -shear dynamo (36). The solid black line is the theoretically predicted maximum growth rate (see Equation 31).

driven turbulence). We will also demonstrate here that, during the second nonlinear phase, the large-scale dynamo is excited by the chiral  $\alpha_\mu$  effect arising in chiral magnetically driven turbulence. The chiral  $\alpha_\mu$  effect was studied using different analytical approaches in Paper I. This effect is due to an interaction of the CME and fluctuations of the small-scale current produced by tangling magnetic fluctuations. These fluctuations are generated by tangling of the large-scale magnetic field through sheared velocity fluctuations. Once the large-scale magnetic field becomes strong enough, the chiral chemical potential decreases, resulting in the saturation of the large-scale dynamo instability.

This situation is similar to that of driving small-scale turbulence via the Bell instability in a system with an external cosmic ray current (Bell 2004; Beresnyak & Li 2014), and the generation of a large-scale magnetic field by the Bell turbulence; see Rogachevskii et al. (2012) for details.

### 4.1. Mean-field theory for large-scale dynamos

In this section, we outline the theoretical predictions for large-scale dynamos based on the mean-field theory (see for details Paper I). The mean induction equation is given by:

$$\frac{\partial \bar{\mathbf{B}}}{\partial t} = \nabla \times [\bar{\mathbf{U}} \times \bar{\mathbf{B}} + (\bar{v}_\mu + \alpha_\mu) \bar{\mathbf{B}} - (\eta + \eta_T) \nabla \times \bar{\mathbf{B}}], \quad (38)$$

where  $\bar{v}_\mu = \eta \bar{\mu}_0$ , and we consider the following equilibrium state:  $\bar{\mu}_{\text{eq}} = \bar{\mu}_0 = \text{const}$  and  $\bar{\mathbf{U}}_{\text{eq}} = 0$ . This mean-field equation contains additional terms caused by turbulence and are related to the chiral  $\alpha_\mu$  effect and the turbulent magnetic diffusivity  $\eta_T$ . In the mean-field equation, the chiral  $v_\mu$  effect is replaced by the mean chiral  $\bar{v}_\mu$  effect. Note, however, that at large fluid and magnetic Reynolds numbers, the  $\alpha_\mu$  effect becomes dominant in comparison with the  $\bar{v}_\mu$  effect.

To study the large-scale dynamo, we seek a solution



to Equation (38) for small perturbations in the form  $\overline{\mathbf{B}}(t, x, z) = \overline{B}_y(t, x, z)\mathbf{e}_y + \nabla \times [\overline{\mathbf{A}}(t, x, z)\mathbf{e}_y]$ , where  $\mathbf{e}_y$  is the unit vector directed along the  $y$  axis. The functions  $\overline{B}_y(t, x, z)$  and  $\overline{\mathbf{A}}(t, x, z)$  are determined by

$$\frac{\partial \overline{\mathbf{A}}(t, x, z)}{\partial t} = (\overline{v}_\mu + \alpha_\mu)\overline{\mathbf{B}}_y + (\eta + \eta_T)\Delta\overline{\mathbf{A}}, \quad (39)$$

$$\frac{\partial \overline{B}_y(t, x, z)}{\partial t} = -(\overline{v}_\mu + \alpha_\mu)\Delta\overline{\mathbf{A}} + (\eta + \eta_T)\Delta\overline{B}_y, \quad (40)$$

where  $\Delta = \nabla_x^2 + \nabla_z^2$ , and other components of the magnetic field are  $\overline{B}_x = -\nabla_z\overline{\mathbf{A}}$  and  $\overline{B}_z = \nabla_x\overline{\mathbf{A}}$ .

We look for a solution of the mean-field Equations (39) and (40) in the form:

$$\overline{\mathbf{A}}, \overline{B}_y \propto \exp[\gamma t + i(k_x x + k_z z)], \quad (41)$$

where the growth rate of the large-scale dynamo instability is

$$\gamma = |(\overline{v}_\mu + \alpha_\mu)k| - (\eta + \eta_T)k^2 \quad (42)$$

with  $k^2 = k_x^2 + k_z^2$ . The maximum growth rate of the large-scale dynamo instability, attained at the wavenumber

$$k \equiv k_\alpha = \frac{|\overline{v}_\mu + \alpha_\mu|}{2(\eta + \eta_T)}, \quad (43)$$

is given by

$$\gamma_\alpha^{\max} = \frac{(\overline{v}_\mu + \alpha_\mu)^2}{4(\eta + \eta_T)} = \frac{(\overline{v}_\mu + \alpha_\mu)^2}{4\eta(1 + \text{Re}_M/3)}. \quad (44)$$

For small magnetic Reynolds numbers,  $\text{Re}_M = u_0\ell_0/\eta = 3\eta_T/\eta$ , this equation yields the correct result for the laminar  $v_\mu^2$  dynamo; see Equation (26).

As was shown in Paper I, the CME in the presence of turbulence gives rise to the chiral  $\alpha_\mu$  effect. The expression for  $\alpha_\mu$  found for large Reynolds numbers and a weak mean magnetic field, is

$$\alpha_\mu = -\frac{2}{3}\overline{v}_\mu \ln \text{Re}_M. \quad (45)$$

Since the  $\alpha_\mu$  effect in homogeneous turbulence is always negative, while the  $\overline{v}_\mu$  effect is positive, the chiral  $\alpha_\mu$  effect decreases the  $\overline{v}_\mu$  effect. Both effects compensate each others at  $\text{Re}_M = 4.5$  (see Paper I). However, for large fluid and magnetic Reynolds numbers,  $\overline{v}_\mu \ll |\alpha_\mu|$ , we can neglect  $\overline{v}_\mu$  in these equations. This case corresponds to the large-scale  $\alpha_\mu^2$  dynamo.

#### 4.2. DNS of chiral magnetically driven turbulence

We have performed a higher resolution ( $576^3$ ) three-dimensional numerical simulation to study chiral magnetically driven turbulence. The chiral Mach number of this simulation is  $\text{Ma}_\mu = 2 \times 10^{-3}$ , the chiral nonlinearity parameter is  $\lambda_\mu = 2 \times 10^{-7}$ , and the magnetic and the chiral Prandtl numbers are unity. The velocity field is initially zero and the magnetic field is Gaussian noise with  $B = 10^{-6}$ .

The time evolution of  $B_{\text{rms}}$ ,  $u_{\text{rms}}$ ,  $\langle \mathbf{A} \cdot \mathbf{B} \rangle$ ,  $\mu_{\text{rms}}$  (multiplied by  $2/\lambda$ ), and  $\langle \mathbf{A} \cdot \mathbf{B} \rangle + 2\mu_{\text{rms}}/\lambda$  of chiral magnetically driven turbulence is shown in the top panel of Figure 8. Here, four phases can be distinguished:

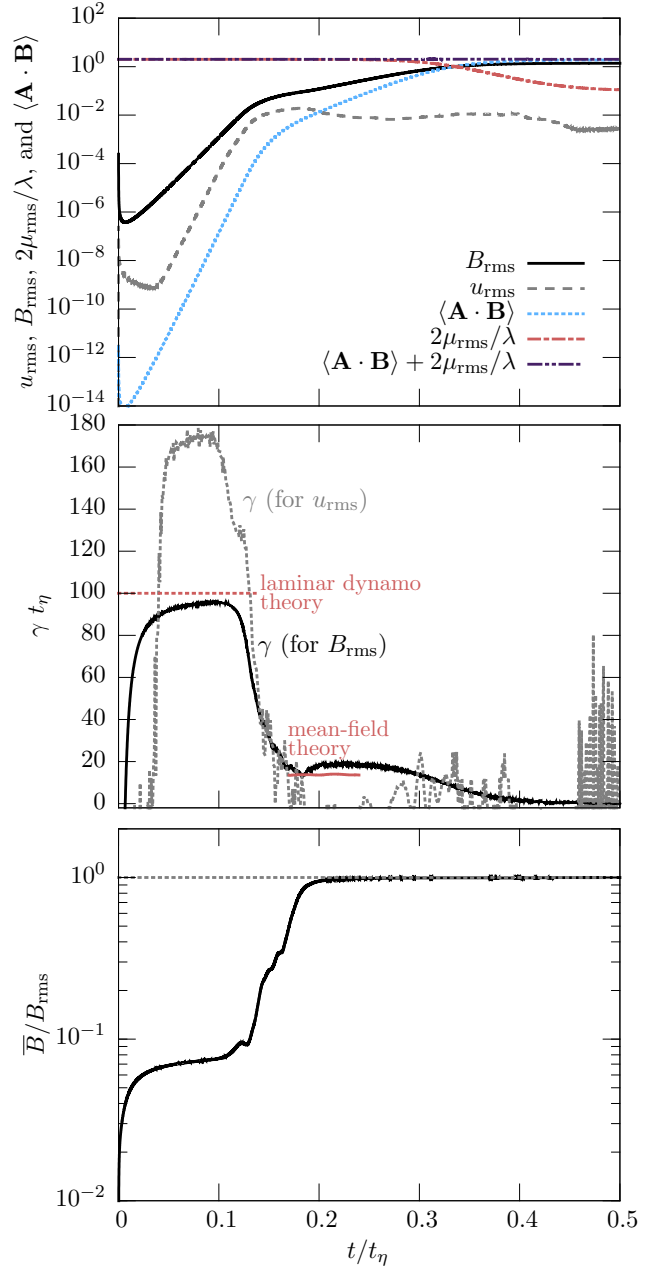


FIG. 8.— **Chiral magnetically driven turbulence.** Time evolution for different quantities.

(1) The kinematic phase of small-scale chiral dynamo instability resulting in exponential growth of small-scale magnetic field due to the CME. This phase ends approximately at  $t = 0.05t_\eta$ .

(2) The first nonlinear phase resulting in production of chiral magnetically driven turbulence. In this phase  $u_{\text{rms}}$  grows from very weak noise over seven orders of magnitude up to nearly equipartition value between turbulent kinetic and magnetic energies, due to the Lorentz force in the Navier-Stokes equation.

(3) The second nonlinear phase resulting in large-scale dynamos. In particular, the evolution of  $B_{\text{rms}}$  for  $t > 0.12t_\eta$  is affected by the velocity field. During this phase the velocity stays approximately constant, while

the magnetic field continues to increase at a reduced growth rate in comparison with that of the small-scale chiral dynamo instability. In this phase, we also observe the formation of inverse energy transfer with a  $k^{-2}$  magnetic energy spectrum that was previously found and comprehensively analysed by Brandenburg et al. (2017b) in DNS of chiral MHD with different parameters.

(4) The third nonlinear phase resulting in saturation of the large-scale dynamos, that ends at  $\approx 0.45t_\eta$  when the large-scale magnetic field reaches the maximum value. The conserved quantity  $\langle \mathbf{A} \cdot \mathbf{B} \rangle + 2\mu_{\text{rms}}/\lambda$  stays constant over all four phases. Saturation is caused by the  $\lambda$  term in the evolution equation of the chiral chemical potential, which leads to a decrease of  $\mu$  from its initial value to 1.

The middle panel of Figure 8 shows the measured growth rate of  $B_{\text{rms}}$  as a function of time. In the kinematic phase,  $\gamma$  agrees with the theoretical prediction for the laminar chiral dynamo instability; see Equation (26), which is indicated by the dashed red horizontal line in the middle panel of Figure 8. During this phase, the growth rate of the velocity field, given by the dotted gray line in Figure 8, is by roughly a factor of two larger than that of the magnetic field. This is expected when turbulence is driven via the Lorentz force, which is quadratic in the magnetic field.

Once the kinetic energy is of the same order as the magnetic energy, the growth rate of the magnetic field decreases abruptly by a factor of more than five. This is expected in the presence of turbulence, because the energy dissipation of the magnetic field is increased by turbulence due to turbulent magnetic diffusion. Additionally, however, a positive contribution to the growth rate comes from the chiral  $\alpha_\mu$  effect that causes large-scale dynamo instability.

The time evolution of the ratio of the mean magnetic field to the total field,  $\bar{B}/B_{\text{rms}}$ , is presented in the bottom panel of Figure 8. The mean magnetic field grows faster than the rms of the total magnetic field in the time interval between 0.14 and 0.2  $t_\eta$ . During this time, the large-scale (mean-field) dynamo operates, so magnetic energy is transferred to larger spatial scales. We now determine directly from DNS the growth rate of the large-scale dynamo using Equation (42). To this end we determine the Reynolds number and the strength of the  $\alpha_\mu$  effect using the data from our DNS. Whereas the rms velocity is a direct output of the simulation, the turbulent forcing scale can be found from analysis of the energy spectra. The theoretical value based on these estimates at the time 0.2  $t_\eta$  is indicated as the solid red horizontal line in the middle panel of Figure 8.

The evolution of kinetic and magnetic energy spectra is shown in Figure 9. We use equal time steps between the different spectra, covering the whole simulation time. The magnetic energy, indicated by blue lines, increases initially at  $k = \mu_0/2 = 10$ , which agrees with the theoretical prediction for the chiral laminar dynamo. The magnetic field drives turbulent kinetic energy, as can clearly be seen in the spectra (indicated by black lines in Figure 9). The final spectral slope of the turbulent kinetic energy is roughly  $-5/3$ . The magnetic field continues to grow at small wavenumbers, producing a peak at  $k = 1$  in the final stage of the time evolution.

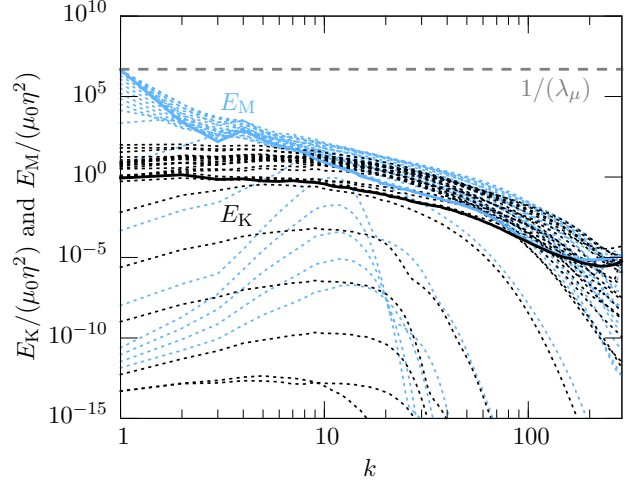


FIG. 9.— **Chiral magnetically driven turbulence.** Magnetic (blue lines) and kinetic (black lines) energy spectra calculated at equal time differences, and the very last spectra shown as solid lines.

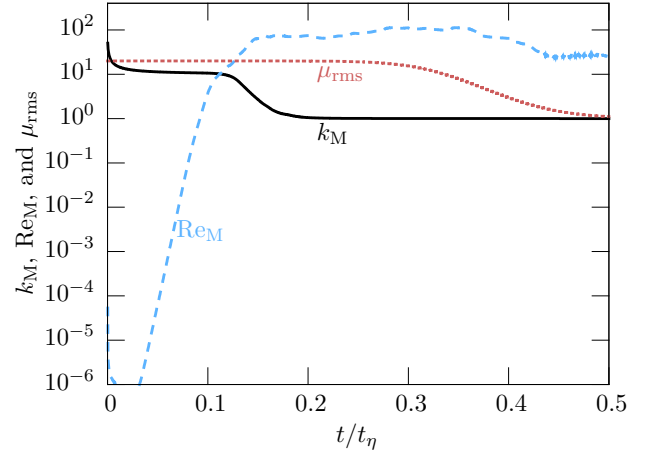


FIG. 10.— **Chiral magnetically driven turbulence.** The black solid line shows the inverse correlation length,  $k_M$ , of the magnetic energy, defined by Equation (46), as a function of time  $t$ . Using this wavenumber and the rms-velocity, the fluid and magnetic Reynolds number are estimated (see Equation 47), that is shown by dashed blue line.

We determine the correlation length of the magnetic field from the magnetic energy spectrum via

$$\xi_M(t) \equiv k_M^{-1}(t) = \frac{1}{\mathcal{E}_M(t)} \int k^{-1} E_M(k, t) dk. \quad (46)$$

Thus the defined  $k_M$  coincides (up to a numerical factor of order unity) with the so-called tracking solution,  $\Delta\mu_{\text{tr}}$  of Boyarsky et al. (2012). There it was demonstrated that in the course of temporal evolution the chiral chemical potential follows  $k_M(t)$ . And indeed, the evolution of  $k_M$ , shown in Figure 10, starts at around 10 (the value of  $\mu_0/2$  in this simulation) and then decreases to  $k_M = k_1$  (corresponding to the simulation box size) at  $t \approx 0.18 t_\eta$ . Interestingly, the chemical potential is affected by magnetic helicity only at much later times, as can be seen in Figure 10. Based on the wavenumber,  $k_M$ , we estimate

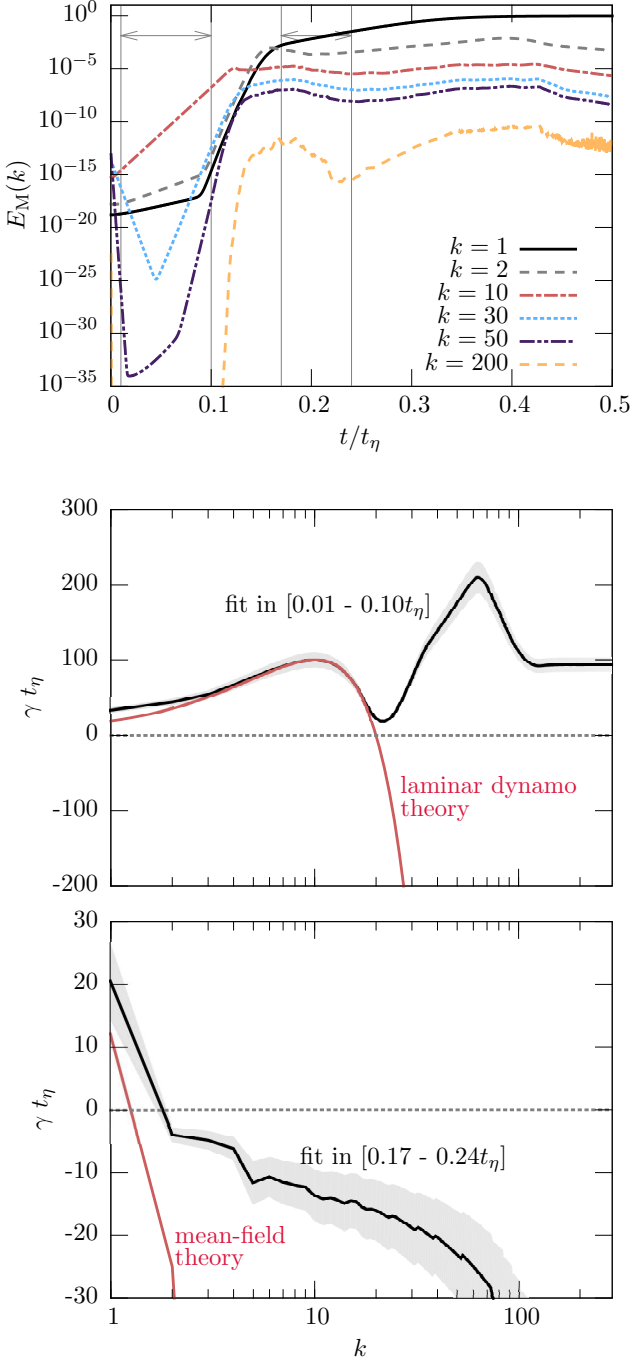


FIG. 11.— **Chiral magnetically driven turbulence.** The evolution of the magnetic energy  $E_M$  on different wavenumbers  $k$  (top panel). The growth rate as a function of  $k$  in different time intervals as given in the plot legend. The black line corresponds to a fit, while the theoretical expectations are given as a red line.

the Reynolds numbers as

$$\text{Re}_M = \text{Re} = \frac{u_{\text{rms}}}{\nu k_M}. \quad (47)$$

Figure 10 shows that the Reynolds number increases exponentially, mostly due to the fast increase of  $u_{\text{rms}}$ , and saturates later at  $\text{Re}_M \approx 10^2$ . Similarly, the turbulent

diffusivity can be estimated as

$$\eta_T = \frac{u_{\text{rms}}}{3 k_M}. \quad (48)$$

During the operation of the mean-field large-scale dynamo, we find  $\eta_T \approx 2.4 \times 10^{-3}$ , which is about 24 times larger than the molecular diffusivity  $\eta$ . Using these estimates, we determine the chiral magnetic  $\alpha_\mu$  effect from Equation (45). The large-scale dynamo growth rate (42) is shown as the solid red horizontal line in the middle panel of Figure 8 and is in agreement with the DNS results shown as the black solid line.

Further analysis of the evolution of the magnetic field at different wavenumbers is presented in Figure 11. In the top panel we show the magnetic energy at various wavenumbers as a function of time. In the kinematic phase, for  $t < 0.1 t_\eta$ , the fastest amplification occurs on  $k = 10$ , as can also be seen in the energy spectra. At  $t \approx 0.18 t_\eta$ , the magnetic field grows only at  $k = 1$ . This confirms the occurrence of a large-scale (mean-field) dynamo. In the next two panels, we compare the observed growth rates as a function of wavenumber at different time intervals. The middle panel of Figure 11 shows the growth rate in the laminar phase, where we find good agreement with the theoretical predictions below  $k \approx 20$ . The resulting value for the growth rate depends on the accuracy of the fitting, and a typical error of ten percent is shown by a gray uncertainty band in the middle panel of Figure 11. Also, the observed growth rate of the mean-field dynamo, which we find from fitting growth rates in the time interval  $0.17\text{--}0.24 t_\eta$ , is comparable to the prediction from mean-field theory using our estimates for the Reynolds number (47) and the turbulent diffusivity (48). As the mean-field dynamo phase is followed by the nonlinear phase, the growth rate is more sensitive to the fitting regime. Hence we indicate a thirty percent uncertainty band for this case. The time intervals for the two different fitting regimes are indicated by gray arrows in the top panel.

#### 4.3. The effect of strong initial magnetic field

The effect of changing the chiral nonlinearity parameter  $\lambda_\mu$  is explored in Brandenburg et al. (2017b), who considered values between  $2 \times 10^{-6}$  and 200. Using dimensional analysis and simulations, it has been shown there that the extent of the inertial range of the turbulence is approximately  $\lambda_\mu^{-1/2}/4$ . The ratio  $\mu/k_\lambda$  is approximately 660 in our reference run for chiral magnetically driven turbulence which was presented in the last section.

Brandenburg et al. (2017b) found that  $E_M(k, t)$  is limited from above by the value of  $\mu/\lambda$ . It is interesting to note that this also applies when the initial magnetic field strength exceeds this limit. To demonstrate this, we now present a simulation with an initial magnetic energy spectrum  $\propto k^4$  for  $k/k_1 < 60$  and exponential decrease for larger  $k$  with  $v_A/c_s = 0.089$ . We use  $\mu_0 = 40$ ,  $\eta = 5 \times 10^{-5}$ ,  $\bar{\rho}\lambda = 8 \times 10^8$ ,  $\text{Ma}_\mu = 0.0014$  and  $\lambda_\mu = 2$ . The result is shown in Figure 12.

At early times,  $E_M/(\eta^2 \mu_0)$  overshoots the value of  $(\mu/\lambda)/(\eta^2 \mu_0) = 1/\lambda_\mu$ , but after a short time it follows this limit almost precisely. This shows that the limit on  $E_M(k, t)$  is obeyed even when the initial field strength

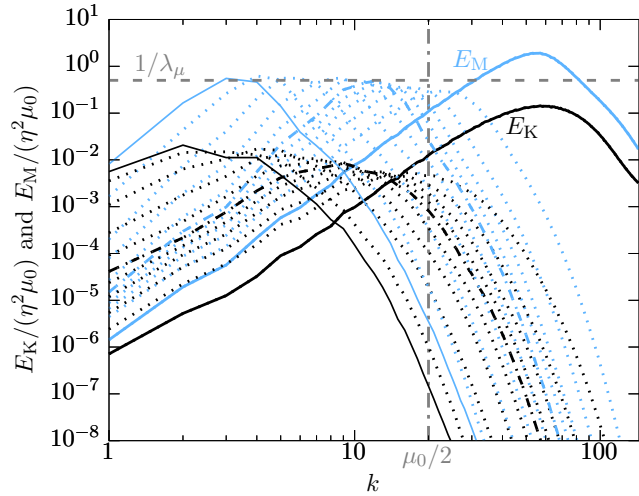


FIG. 12.— **Chiral magnetically driven turbulence.** Evolution of the magnetic (blue lines) and kinetic (black lines) energy spectrum for a run with large initial magnetic field on a small spatial scale. The initial spectra are shown as thick solid lines; later spectra have equal time intervals up to  $0.025 t_\eta$  (shown in thick dashed lines). Above  $t = 0.025 t_\eta$ , the time intervals increase by a factor of two, until the final spectra are reached presented here as thin solid lines. The horizontal dashed gray line shows  $1/\lambda_\mu$ , the upper limit predicted by the chiral conservation law, and the vertical gray line shows the scale where the growth rate of the small-scale chiral instability reaches its maximum.

exceeds this value.

#### 4.4. Stages of chiral magnetically driven turbulence

This DNS demonstrated that the magnetic field evolution proceeds in the following distinct stages:

- (1) Small-scale chiral dynamo instability.
- (2) First nonlinear stage when the Lorentz force drives small-scale turbulence.
- (3) Formation of inverse energy transfer with a  $k^{-2}$  magnetic energy spectrum; see [Brandenburg et al. \(2017b\)](#) for details.
- (4) Generation of large-scale magnetic field by chiral magnetically driven turbulence.
- (5) Decrease of the chemical potential and saturation of the large-scale chiral dynamo.

Although the magnetic field cannot grow any further, the spectrum continues to move to smaller wavenumbers in a shape-invariant fashion (cf. [Brandenburg & Kahniashvili 2017](#)). This implies that the magnetic integral scale  $\xi_M \equiv k_M^{-1}$  continues to grow and the magnetic energy continues to decline proportional to  $t^{-2/3}$  such that  $\langle \mathbf{B}^2 \rangle_{\xi_M} \approx \text{const}$ .

### 5. DNS OF LARGE-SCALE DYNAMOS IN FORCED, NONHELICAL, AND HOMOGENEOUS TURBULENCE

In this section we study the evolution of the magnetic field in the presence of forced, nonhelical, and homogeneous turbulence to control the turbulence parameters in the chiral MHD simulations. Chiral dynamos in forced turbulence can be described by the mean-field chiral MHD equations. The theoretical results related to the mean-field chiral dynamos obtained in Paper I have been outlined in Section 4.1.

#### 5.1. DNS setup for externally forced turbulence

TABLE 3  
OVERVIEW OF RUNS WITH EXTERNALLY FORCED TURBULENCE.

	$\mu_0$	$\frac{\text{Ma}_\mu}{10^{-3}}$	$\frac{\lambda_\mu}{10^{-6}}$	$\frac{k_\lambda}{\mu_0}$	$\frac{k_{\text{diff}}}{\mu_0}$	$k_f$	$\text{Re}_M$ (early $\rightarrow$ late)
Ta2-1	20	8	16	160	4.5	10	24 $\rightarrow$ 19
Ta2-2	20	4	4.0	80	63	10	36 $\rightarrow$ 28
Ta2-3	20	8	16	160	45	10	16 $\rightarrow$ 14
Ta2-4	20	4	4.0	80	63	10	4 $\rightarrow$ 13
<b>Ta2-5</b>	<b>20</b>	<b>8</b>	<b>160</b>	<b>51</b>	<b>80</b>	<b>10</b>	<b>24 <math>\rightarrow</math> 18</b>
Ta2-6	20	8	1.6	51	80	10	16 $\rightarrow$ 14
Ta2-7	30	12	32	230	38	4	42 $\rightarrow$ 58
Ta2-8	30	9	18	160	43	4	58 $\rightarrow$ 65
Ta2-9	30	9	13.5	150	47	4	82 $\rightarrow$ 74
Ta2-10	40	8	16	160	45	4	119 $\rightarrow$ 107

To study chiral large-scale dynamos, we perform three-dimensional DNS with externally forced turbulence and a spatial resolution of  $200^3$ . In run Ta2-10, the resolution is  $280^3$  (see Table 3). Turbulence is driven via the forcing term  $\mathbf{f}(\mathbf{x}, t)$  in Equation (2). The forcing function is nonhelical and localized around the wavenumber  $k_f$ ; see [Haugen et al. \(2004\)](#) for details. For the runs presented in the present paper, we choose  $k_f = 4$  and 10. These values are small enough so that the fluid and magnetic Reynolds numbers,  $\text{Re} = u_{\text{rms}}/(\nu k_f)$  and  $\text{Re}_M = u_{\text{rms}}/(\eta k_f)$ , are sufficiently large for turbulence to develop. At the same time,  $k_f$  is large enough for a clear separation between the box scale and the forcing scale, allowing the study of mean-field (large-scale) dynamos. In the numerical simulations we vary  $\text{Ma}_\mu$ ,  $\lambda_\mu$ , and  $\text{Re}$  (see Table 3).

For comparison with the results from mean-field theory, the simulations need to fulfill the following criteria:

- To capture the maximum amplification inside the numerical domain with  $k_{\text{box}} = 2\pi/L_{\text{box}} = 1$ , the condition  $k_{\text{max}} > 1$  needs to be fulfilled. As shown in Equation (43),  $k_{\text{max}}$  is proportional to  $\eta/\eta_T$ , which is inversely proportional to the magnetic Reynolds number  $\text{Re}_M$ . As a result, the chemical potential needs to be sufficiently high for  $k_{\text{max}} > 1$ .
- Due to non-local effects, the turbulent diffusivity  $\eta_T$  is generally scale-dependent and decreases above  $k_f$  ([Brandenburg et al. 2008](#)). For comparison with mean-field theory, the chiral dynamo instability has to occur on scales  $k < k_f$ , where  $\eta_T \approx u_{\text{rms}}/(3k_f)$ . Note, however, that the presence of a mean kinetic helicity in the system caused by the CME (see Paper I), can increase the turbulent diffusivity  $\eta_T$  for moderate magnetic Reynolds numbers by up to 50% ([Brandenburg et al. 2017a](#)).
- To simplify the system, we avoid classical small-scale dynamo action, which occurs at magnetic Reynolds numbers larger than  $\text{Re}_{M, \text{crit}} \approx 50$ .

#### 5.2. DNS of chiral dynamos in forced turbulence

The time evolution of different quantities in our reference run is presented in Figure 13. The magnetic field increases first exponentially with a growth rate  $\gamma \approx 60 t_\eta^{-1}$ , which is about a factor of 1.6 lower than that expected



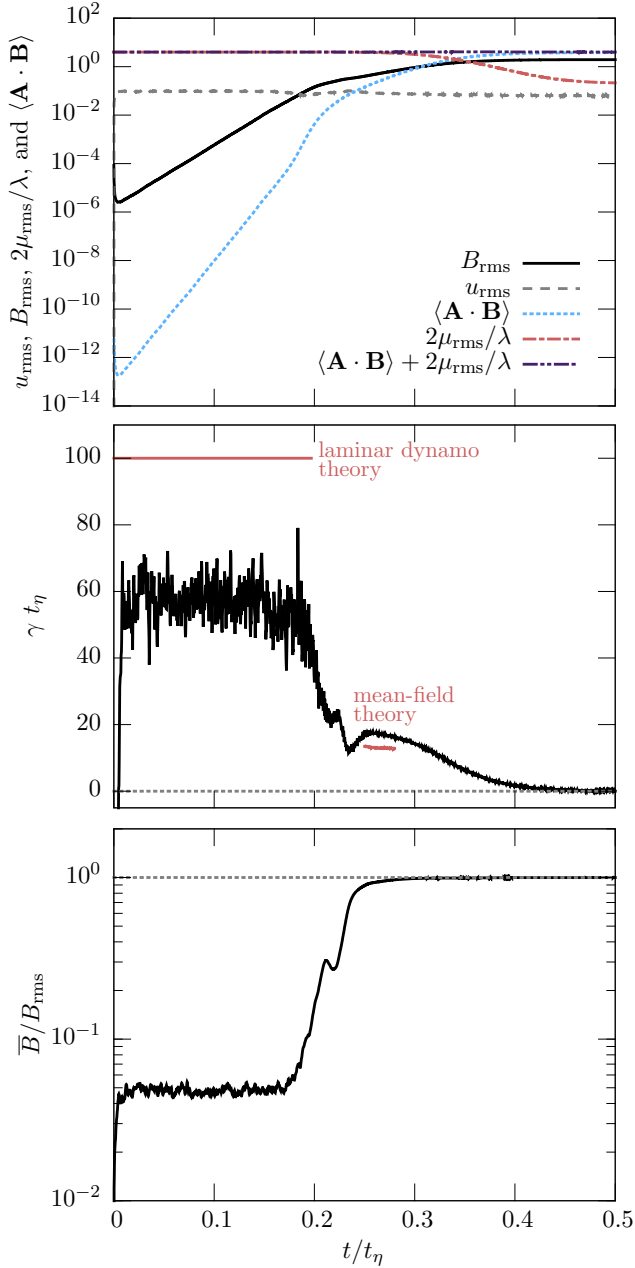


FIG. 13.— **Externally forced turbulence.** Time evolution of the magnetic field, the velocity field, and the chemical potential, as well as the mean value of the magnetic helicity (top panel). The middle panel shows the growth rate of  $B_{\text{rms}}$  as a function of time (solid black line). The red lines are theoretical expectations in different dynamo phases. In the bottom panel the ratio of the mean magnetic field to the total field  $B_{\text{rms}}$  is presented.

for the laminar  $v_\mu^2$  dynamo (see the middle panel of Figure 13). This difference seems to be caused by the presence of a random forcing (see discussion below). At approximately  $0.2 t_\eta$ , the growth rate decreases to a value of  $\gamma \approx 15 t_\eta^{-1}$  that is consistent with that of the mean-field chiral  $\alpha_\mu^2$  dynamo, before saturation occurs at  $0.4 t_\eta$ . The evolution of  $B_{\text{rms}}$  is qualitatively comparable to that for the case of chiral magnetically produced turbulence; see Figure 8. An additional difference to the latter case is the value of  $u_{\text{rms}} \approx 0.1$  for the externally forced tur-

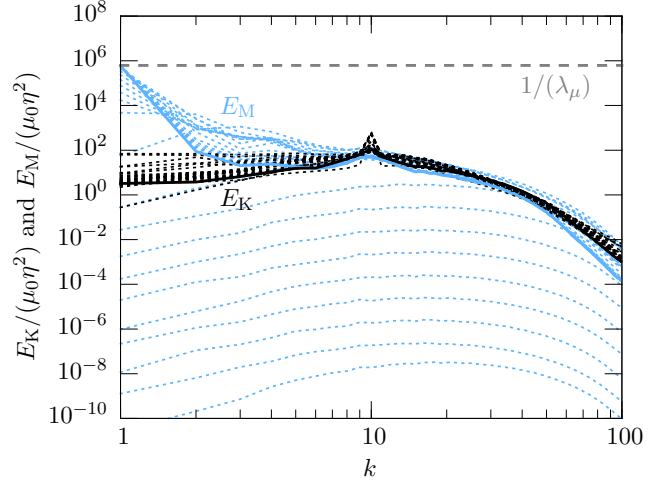


FIG. 14.— **Externally forced turbulence.** Evolution of kinetic (black lines) and magnetic energy spectra (blue lines) for the reference run Ta2-5. The ratio  $\mu_0/\lambda$  is indicated by the horizontal dashed line.

bulence, that is controlled by the intensity of the forcing function. An indication of the presence of a mean-field dynamo is the evolution of  $\bar{B}/B_{\text{rms}}$  in the bottom panel of Figure 13, which reaches a value of unity at  $0.3 t_\eta$ .

The energy spectra presented in Figure 14 support the large-scale dynamo scenario. First, the magnetic energy increases at all scales, and at later times the maximum of the magnetic energy transfers to smaller wavenumbers, finally producing a clear peak at  $k = 1$ , i.e., the smallest wavenumber in our periodic domain.

A detailed analysis of the growth of magnetic energy is presented in Figure 15. In the first phase, the growth rate of the magnetic field is independent of the wavenumber  $k$  (see top panel), due to a coupling between different modes. The growth rate measured in this phase is less than that in the laminar case (see middle panel) due to a scale-dependent turbulent diffusion caused by the random forcing.

Within the time interval  $(0.22-0.28) t_\eta$ , only the magnetic field at  $k = 1$  increases. This is clearly seen in the bottom panel of Figure 15, where we show the evolution of the magnetic energy at different wavenumbers  $k$ . The growth rate of the mean-field dynamo, which is determined at  $k = 1$ , agrees with the result from mean-field theory, given by Equation (49). There is a small dependency of the resulting mean-field growth rate on the exact fitting regime. Especially in cases where the phase of the mean-field dynamo is very short, changing the fitting range can affect the result by a factor up to 30%. We use the latter value as an estimate of the uncertainty in the growth rate, and additionally indicate an error of 20% in determining of the Reynolds number, that is caused by the temporal variations of  $u_{\text{rms}}$ .

### 5.3. Dependence on the magnetic Reynolds number

Based on the mean-field theory developed in Paper I, we expect the following. Using the expression for the  $\alpha_\mu$  effect given by Equation (45), the maximum growth rate (44) for the mean-field dynamo can be rewritten as

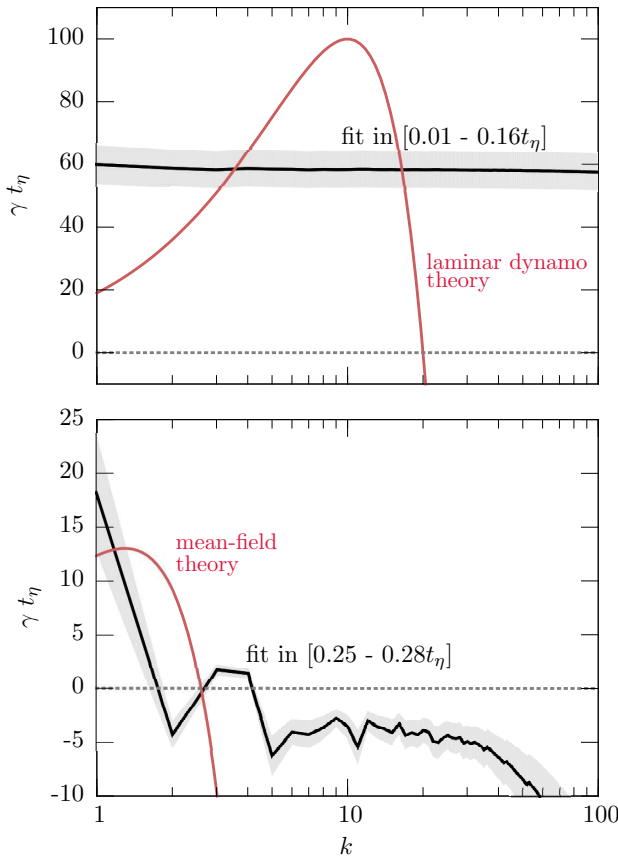
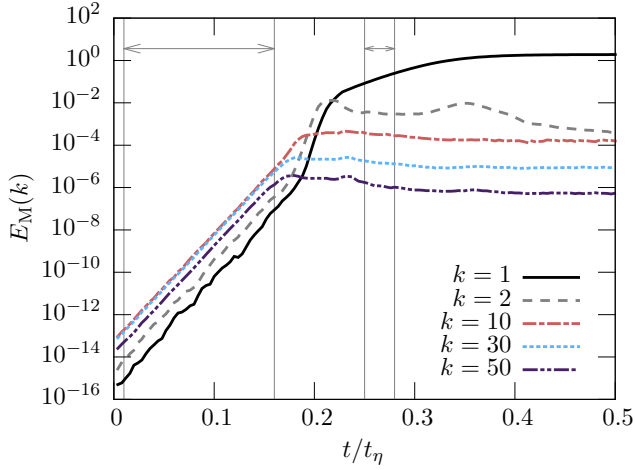


FIG. 15.— **Externally forced turbulence.** Time evolution of the magnetic energy at different wavenumbers  $k$  (top panel). The remaining panels show the growth rates as a function of scale in different fit intervals.

a function of the magnetic Reynolds number:

$$\gamma_{\max}(\text{Re}_M) = \frac{\bar{v}_\mu^2 (1 - 2/3 \ln \text{Re}_M)^2}{4\eta (1 + \text{Re}_M/3)}, \quad (49)$$

where the ratio  $\eta_T/\eta = \text{Re}_M/3$ .

We perform DNS with different Reynolds numbers to test the scaling of  $\gamma_{\max}(\text{Re}_M)$  given by Equation (49). The parameters of the runs with externally forced turbulence are summarized in Table 3. We vary  $\nu (= \eta)$ ,

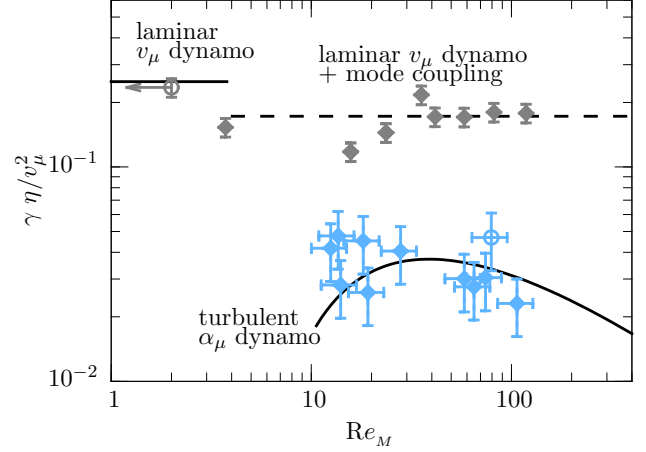


FIG. 16.— **Externally forced turbulence and chiral magnetically driven turbulence.** The normalized growth rate  $\gamma \eta/v_\mu^2$  of the magnetic field as a function of the magnetic Reynolds number  $\text{Re}_M$ . The gray data points show the growth rate in the initial, purely kinematic phase of the simulations. The blue data points show the measured growth rate of the magnetic field on  $k = 1$ , when the large-scale dynamo occurs. The diamond-shaped data points represent simulations of forced turbulence, while the dot-shaped data points refer to the case of chiral magnetically driven turbulence. The growth rate observed in the initial laminar phase for the case of chiral magnetically driven turbulence is shown at  $\text{Re}_M = 2$ , with the left arrow indicating that the actual  $\text{Re}_M$  is much lower and out of the plot range at this time; see Figure 10.

the forcing wavenumber  $k_f$ , as well as the amplitude of the forcing, to determine the function  $\gamma_{\max}(\text{Re}_M)$ . In the initial phase,  $u_{\text{rms}}$  is constant in time. Once large-scale turbulent dynamo action occurs, there are additional minor variations in  $u_{\text{rms}}$ , because the system is already in the nonlinear phase. The nonlinear terms in the Navier-Stokes equation lead to a modification of the velocity field at small spatial scales, which affects the value of  $u_{\text{rms}}$  and results in the small difference between the initial and final values of the Reynolds numbers (see Table 3).

According to Equation (43), the wavenumber associated with the maximum growth rate of the large-scale turbulent dynamo instability decreases with increasing  $\text{Re}_M$ . In order to keep this mode inside the computational domain and hence to compare the measured growth rate with the maximum one given by Equation (49), we vary the value of  $\mu_0$  in our simulations. The variation of  $\mu_0$  and the additional variation of  $\eta$  for scanning through the  $\text{Re}_M$  parameter space, implies that  $\text{Ma}_\mu$  changes correspondingly.

The values of the nonlinear parameter  $\lambda$  should be within a certain range. Indeed, the saturation value of the magnetic field, given by Equation (28), is proportional to  $\lambda^{-1/2}$ . In order for the Alfvén velocity not to exceed the sound speed,  $\lambda$  should not be below a certain value. On the other hand,  $\lambda$  should not be too large, as in this case the dynamo would saturate quickly and there is only a very short time interval of the large scale dynamo. In this case, determining the growth rate of the mean-field dynamo, and hence comparing with the mean-field theory, is difficult.

In Figure 16 we show the normalized growth rate

$\gamma \eta/v_\mu^2$  of the magnetic field as a function of the magnetic Reynolds number  $\text{Re}_M$ . The gray data points show the growth rate in the initial, purely kinematic phase of the simulations. The blue data points show the measured growth rate of the magnetic field on  $k = 1$ , when the large-scale dynamo occurs. For comparison of the results with externally forced turbulence (indicated as diamond-shaped data points), we show in Figure 16 also the results obtained for the dynamo in chiral magnetically driven turbulence, which are indicated as dots.

In DNS with externally forced turbulence, we see in all cases a reduced growth rate due to mode coupling. Contrary to the case with externally forced turbulence, in DNS with the chiral magnetically driven turbulence we do initially observe the purely laminar dynamo with the growth rate given by Equation (26), because there is no mode coupling in the initial phase of the magnetic field evolution in this case. On the other hand, the measured growth rates of the mean-field dynamo in both cases agree (within the error bars) with the growth rates obtained from the mean-field theory.

## 6. CHIRAL MHD DYNAMOS IN ASTROPHYSICAL RELATIVISTIC PLASMAS

In this section, the results for the nonlinear evolution of the chiral chemical potential, the magnetic field, and the turbulence found in this paper are applied to astrophysical relativistic plasmas. We begin by discussing the role of chiral dynamos in the early Universe and identify conditions under which the CME affects the generation and evolution of cosmic magnetic fields. Finally, we examine in Section 6.2 the importance of the CME in proto-neutron stars.

### 6.1. Early Universe

In spite of many possible mechanisms that can produce magnetic fields in the early Universe (see e.g. Widrow 2002; Widrow et al. 2012; Durrer & Neronov 2013; Giovannini 2004; Subramanian 2016, for review), the origin of cosmic magnetic fields remains an open question. Their generation is often associated with non-equilibrium events in the Universe (e.g. inflation or phase transitions). A period of particular interest is the electroweak (EW) epoch characterized by temperatures of  $10^{15}$  K ( $k_B T \sim 100$  GeV). Several important events take place around this time: the electroweak symmetry gets broken, photons appear while intermediate vector bosons become massive, and the asymmetry between matter and anti-matter appears. Magnetic fields of appreciable strength can be generated as a consequence of these events (Vachaspati 1991; Olesen 1992; Enqvist & Olesen 1993; Enqvist 1994; Vachaspati & Field 1994; Gasperini et al. 1995; Davidson 1996; Baym et al. 1996; Vachaspati 2001; Semikoz 2010). Their typical correlation length  $\xi_M^{(\text{ew})} \sim (\alpha_{\text{em}} T)^{-1}$  corresponds to only a few centimeters today – much less than the observed correlation scales of magnetic fields in galaxies or galaxy clusters. Therefore, in the absence of mechanisms that can increase the comoving scale of the magnetic field beyond  $\xi_M^{(\text{ew})}$ , such fields were deemed to be irrelevant to the problem of cosmic magnetic fields (for discussion see e.g. Durrer & Caprini 2003; Caprini et al. 2009;

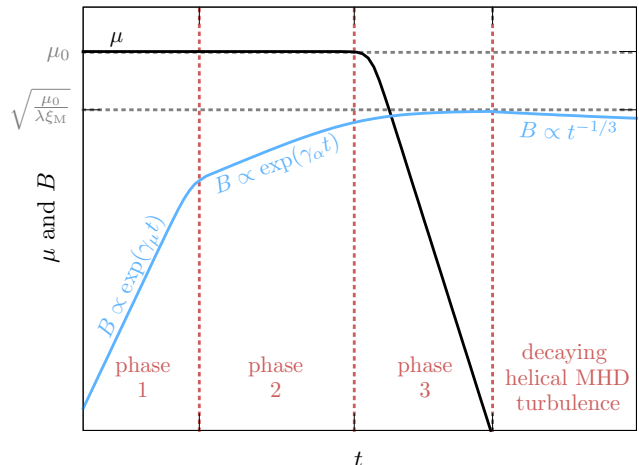


FIG. 17.— **Chiral MHD dynamos in the early Universe.** Sketch of the different phases of the chiral mean-field dynamo. From left to right: small-scale chiral dynamo (phase 1), large-scale turbulent dynamo (phase 2), and saturation (phase 3). After saturation of the dynamo, the magnetic magnetic field dissipates. The upper horizontal dotted line shows the initial value of  $\mu$  and the lower one the “saturation limit”, given by Eq. (58).

Saveliev et al. 2012; Kahniashvili et al. 2013b).

The situation may change if (i) the magnetic fields are helical and (ii) the plasma is turbulent. In this case, an inverse transfer of magnetic energy may develop which leads to a shift of the typical scale of the magnetic field to progressively larger scales (Brandenburg et al. 1996; Christensson et al. 2001; Banerjee & Jedamzik 2004; Kahniashvili et al. 2013b). The origin of such turbulence has been unknown. An often considered paradigm is that a random magnetic field, generated at small scales, produces turbulent motions via the Lorentz force. However, continuous energy input is required. If this is not the case, the magnetic field decays:  $\langle \mathbf{B}^2 \rangle \sim t^{-2/3}$  as the correlation scale grows (Biskamp & Müller 1999; Kahniashvili et al. 2013b), so that  $\langle \mathbf{B}^2 \rangle \xi_M = \text{const}$ .

In the present work, we demonstrated that the presence of a finite chiral charge in the plasma at the EW epoch is sufficient to satisfy the above requirements (i) and (ii). As a result

- (1) helical magnetic fields are excited,
- (2) turbulence with large  $\text{Re}_M$  is produced, and
- (3) the comoving correlation scale increases.

We discuss each of these phases in details below.

#### 6.1.1. Generation and evolution of cosmic magnetic fields in the presence of a chiral chemical potential

Although it is not possible to perform numerical simulations with parameters matching those of the early Universe, the results of the present paper allow us to make qualitative predictions about the fate of cosmological magnetic fields generated at the EW epoch in the presence of a chiral chemical potential.

All the main stages of the magnetic field evolution, summarized in Section 4.4, can occur in the early Universe (a sketch of the main phases is provided in Figure 17).

**Phase 1.** At this initial stage, the small-scale chiral dynamo instability develops at scales around  $\xi_\mu$ , where

$$\xi_\mu \equiv \frac{2}{|\mu_0|}, \quad (50)$$

and

$$\mu_0 \approx 4\alpha_{\text{em}} \frac{\mu_5}{\hbar c} \approx 1.5 \times 10^{14} \text{ cm}^{-1} \frac{\mu_5}{100 \text{ GeV}}. \quad (51)$$

The chemical potential  $\mu_5$  can be approximated by the thermal energy  $k_B T$  for order of magnitude estimates. In what follows, we provide numerical estimates for  $\mu_5 = 100 \text{ GeV}$  which corresponds to the typical thermal energy of relativistic particles at the EW epoch. The characteristic energy at the quantum chromodynamics phase transition is  $\approx 100 \text{ MeV}$  where the quark-gluon plasma turns into hadrons.

The growth rate of an initially weak magnetic field in the linear stage of the chiral dynamo instability is given by Equation (26):

$$\gamma_\mu^{\text{max}} = \frac{\mu_0^2 \eta}{4} \approx 2.4 \times 10^{19} T_{100}^{-1} \text{ s}^{-1}. \quad (52)$$

For the value of the magnetic diffusivity  $\eta = c^2/(4\pi\sigma)$  in the early Universe, we adopted the conductivity  $\sigma$  from Equation (1.11) of Arnold et al. (2000). Numerically,

$$\eta(T) = 7.3 \times 10^{-4} \frac{\hbar c^2}{k_B T} \approx 4.3 \times 10^{-9} T_{100}^{-1} \text{ cm}^2 \text{ s}^{-1}, \quad (53)$$

where  $T_{100} = 1.2 \times 10^{15} \text{ K}$  (so that  $k_B T_{100} = 100 \text{ GeV}$ ). As a result, the number of  $e$ -foldings over one Hubble time  $t_H$  is

$$\gamma_\mu^{\text{max}} t_H \gg 1,$$

where

$$t_H = H^{-1}(T) \approx 4.8 \times 10^{-11} g_{100}^{-1/2} T_{100}^{-2} \text{ s} \quad (54)$$

(here  $g_*$  is the number of relativistic degrees of freedom and  $g_{100} = g_*/100$ ). We should stress that this picture has been known before and was described in many previous works (Joyce & Shaposhnikov 1997; Fröhlich & Pedrini 2000, 2002; Boyarsky et al. 2012).

In this regime one could reach  $\mathcal{O}(10^9)$   $e$ -folds over the Hubble time  $t_H$ . However, as shown in this work, already after a few hundred  $e$ -foldings, the magnetic field starts to excite turbulence via the Lorentz force. This happens once the magnetic field is no longer force-free. Once the flow velocities reach the level  $v_\mu = \mu_0 \eta$ , nonlinear terms are no longer small, small-scale turbulence is produced, and the next phase begins.

**Phase 2.** The subsequent evolution of the magnetic field depends on the strength of the chiral magnetically excited turbulence. This has been shown through the mean-field analysis of Rogachevskii et al. (2017) and is confirmed by the present work; see e.g. Figure 16. The growth rate and instability scale depend on the magnetic Reynolds number; see Equations (42)–(44). The maximum growth rate for  $\text{Re}_M \gg 1$  is given by

$$\gamma_\alpha^{\text{max}} = \gamma_\mu^{\text{max}} \frac{4}{3} \frac{(\log \text{Re}_M)^2}{\text{Re}_M}, \quad (55)$$

where  $\gamma_\mu^{\text{max}}$  is given by Equation (52). For the early Universe, the exact value of the magnetic Reynolds number is impossible to determine from the numerical simulations, but one expects  $\text{Re}_M \gg 1$  and we show in Figure 18 that in a wide range of magnetic Reynolds numbers,  $1 \ll \text{Re}_M \ll 6 \times 10^{12}$ , the number of  $e$ -foldings

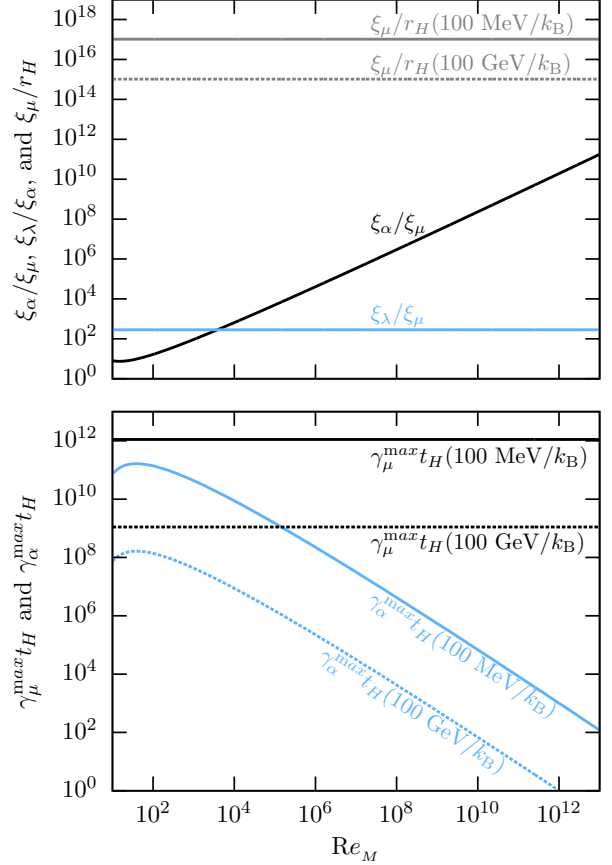


FIG. 18.— **Chiral MHD dynamos in the early Universe.** The ratios between  $\xi_\alpha$  of the turbulence-driven dynamo (Eq. (43)) and scale  $\xi_\mu$  (Equation (50)), as well as the ratio between  $\xi_\mu$  and the Hubble radius at different temperatures. In the top panel, furthermore, the ratio  $\xi_\mu/\xi_\lambda$  is presented. Maximal growth rates over the Hubble time for laminar ( $\gamma_\mu^{\text{max}}$ ) and turbulent ( $\gamma_\alpha^{\text{max}}$ ) regimes are shown in the bottom panel.

during one Hubble time is much larger than 1. The turbulence efficiently excites magnetic fields at scales much larger than  $\xi_\mu$  (Figure 18, top panel).

Using dimensional analysis and DNS, Brandenburg et al. (2017b) demonstrated that the resulting spectrum of the magnetic fields behaves as  $E_M \propto k^{-2}$  between  $k_\mu$  and  $k_\lambda$ , given by Equation (20). The wavenumber  $k_\lambda$  depends on the nonlinearity parameter  $\lambda$ , defined by Equation (5), which, in the early Universe, is given by

$$\lambda = 3\hbar c \left( \frac{8\alpha_{\text{em}}}{k_B T} \right)^2 \approx 1.3 \times 10^{-17} T_{100}^{-2} \text{ cm erg}^{-1} \quad (56)$$

and on the mean density of the plasma

$$\bar{\rho} = \frac{\pi^2}{30} g_* \frac{(k_B T)^4}{\hbar^3 c^5} \approx 7.6 \times 10^{26} g_{100} T_{100}^4 \text{ g cm}^{-3}. \quad (57)$$

The ratio  $\xi_\lambda/\xi_\mu = k_\mu/k_\lambda$  is presented in the top panel of Figure 18, but we note that the exact numerical coefficient in the condition  $k_\mu/k_\lambda \gg 1$  might depend on  $\text{Re}_M$ .

**Phase 3.** The stage of large-scale turbulent dynamo action ends with the *saturation phase* (see Section 4.4 and Figure 17). At this stage the total chiral charge



(determined by the initial conditions) gets transferred to magnetic helicity. As shown by [Boyersky et al. \(2012\)](#) (see also [Joyce & Shaposhnikov \(1997\)](#) for the earlier work as well as [Tashiro et al. \(2012\)](#) and [Hirono et al. \(2015\)](#) for more discussion), and confirmed by numerical simulations in [Brandenburg et al. \(2017b\)](#) and in the present work, the chiral chemical potential  $\mu$  at this stage follows  $k_M$  and thus decreases with time. Therefore, most of the chiral charge will be transferred with time into magnetic helicity,

$$\langle \mathbf{A} \cdot \mathbf{B} \rangle \simeq \xi_M \langle \mathbf{B}^2 \rangle \rightarrow \frac{2\mu_0}{\lambda}, \quad (58)$$

switching off the CME (the end of “Phase 3” in [Figure 17](#)).

### 6.1.2. Chiral MHD and cosmic magnetic fields

Magnetic fields produced by chiral dynamos are fully helical. This implies that, when the CME has become negligible, the subsequent phase of decaying helical turbulence begins and the magnetic energy decreases, while the magnetic correlation length increases in such a way that the magnetic helicity (58) is conserved for very small magnetic diffusivity ([Biskamp & Müller 1999](#); [Kahniashvili et al. 2013b](#)).

Based on Equation (58), one can estimate the magnetic helicity *today*; see also [Brandenburg et al. \(2017b\)](#). Taking as an estimate for the chiral chemical potential  $\mu_5 \sim k_B T$  (this means that the density of the chiral charge is of the order of the number density of photons), one finds:

$$\langle \mathbf{B}^2 \rangle_{\xi_M} \simeq \frac{\hbar c}{4\alpha_{em}} \frac{g_0}{g_*} n_\gamma^{(0)} \simeq 6 \times 10^{-38} \text{ G}^2 \text{ Mpc}. \quad (59)$$

Here the present number density of photons is  $n_\gamma^{(0)} = 411 \text{ cm}^{-3}$ , and the ratio  $g_0/g_* \approx 3.36/106.75$  of the effective relativistic degrees of freedom today and at the EW epoch appears, because the photon number density dilutes as  $T^3$  while the magnetic helicity dilutes as  $a^{-3}$ . We recall that, to arrive at the numerical value in  $\text{G}^2 \text{ Mpc}$  given in Equation (59), an additional  $4\pi$  factor was applied to convert to Gaussian units.

Under the assumption that the spectrum of the cosmic magnetic field is sharply peaked at some scale  $\xi_0$  (as is the case in all the simulations presented here), the lower bounds on magnetic fields, inferred from the non-observation of GeV cascades from TeV sources ([Neronov & Vovk 2010](#); [Tavecchio et al. 2010](#); [Dolag et al. 2011](#)) can be directly translated into a bound on magnetic helicity today. The observational bound scales as  $|\mathbf{B}| \propto \xi_0^{-1/2}$  for  $\xi_0 < 1 \text{ Mpc}$  ([Neronov & Vovk 2010](#)) and therefore  $\langle \mathbf{B}^2 \rangle_{\xi_0} = \text{const} > 8 \times 10^{-38} \text{ G}^2 \text{ Mpc}$ . The numerical value is obtained using the most conservative bound  $|\mathbf{B}| \geq 10^{-18} \text{ G}$  at 1 Mpc ([Dermer et al. 2011](#), see also [Durrer & Neronov 2013](#)).

The limit given by Equation (59) is quite general. It does not rely on chiral MHD or the chiral magnetic effect, but simply re-interprets the bounds of [Neronov & Vovk \(2010\)](#), [Tavecchio et al. \(2010\)](#), [Dolag et al. \(2011\)](#), and [Dermer et al. \(2011\)](#) as bounds on magnetic helicity. Given such an interpretation, we conclude that *if cosmic magnetic fields are helical and have a cosmological origin, then at some moment in the history of the*

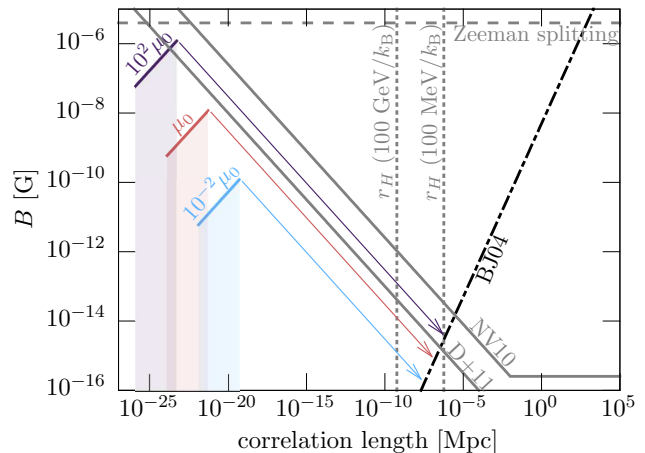


FIG. 19.— **Chiral MHD dynamos in the early Universe.** The magnetic field strength resulting from a chiral dynamo as a function of correlation length in comoving units and comparison with observational constraints. The differently colored lines show the chiral magnetically produced magnetic field strength in the range between the injection length  $\mu^{-1}$  and the saturation length  $k_\lambda^{-1}$ ; see Equations (50) and (20), respectively. The colors indicate different values of the chiral chemical potential: Red refers to the value of  $\mu_0$  given in Equation (51), blue to  $10^{-2}\mu_0$ , and purple to  $10^2\mu_0$ . The dashed gray line is an upper limit on the intergalactic magnetic field from Zeeman splitting. Solid gray lines, refer to the lower limits reported by [Neronov & Vovk \(2010\)](#) (“NV10”) and [Dermer et al. \(2011\)](#) (“D+11”), respectively. The vertical dotted gray lines show the horizon at  $k_B T = 100 \text{ GeV}$  and  $100 \text{ MeV}$  correspondingly. The thin colored arrows refer to the nonlinear evolution of magnetic fields in an inverse cascade in helical turbulence up to the final value as given in [Banerjee & Jedamzik \(2004\)](#) (line “BJ04”).

Universe a density of the chiral charge was much larger than  $n_\gamma(T)$ . This chiral charge can be, for example, in the form of magnetic helicity or of chiral asymmetry of fermions, or both. To generate such a charge density, some new physics beyond the Standard Model of elementary particles is required. Below we list several possible mechanisms that can generate large initial chiral charge density:

(1) The upper bound in Equation (59) assumes that only one fermion of the Standard Model developed a chiral asymmetry  $\sim n_\gamma$ . Many fermionic species are present in the plasma at the electroweak epoch. They all can have left-right asymmetric population of comparable size, increasing the total chirality by a factor  $\mathcal{O}(10)$ , which makes the estimate (59) consistent with the lower bound from [Dermer et al. \(2011\)](#). One should check of course, whether for more massive fermions the chirality flipping rate is much slower than the dynamo growth rate determined by Equation (52).

(2) The estimate (59) assumed that left-right asymmetry was created via thermal processes. Of course, new physics at EW epoch can result in non-thermal production of chiral asymmetry (e.g. via decays of some long-lived particles), thus leading to  $n_5 \gg n_\gamma$  and so increasing the limit (59).

(3) The left-right asymmetry may be produced as a consequence of the decay of helical *hypermagnetic* fields prior to the EW epoch. Such a scenario, relating hypermagnetic helicity to the chiral asymmetry has been discussed previously, e.g. in [Giovannini & Shaposhnikov \(1998\)](#); [Semikoz et al. \(2012\)](#). A conservation law similar

to that of (10) exist also for hypermagnetic fields and the decay of the latter may cause asymmetric population of left and right states.

(4) In our analysis, we have not taken into account the chiral vortical effect (Vilenkin 1979). For nonvanishing chemical potential, it leads to an additional current along the direction of vorticity (see, e.g., Tashiro et al. 2012).

From the point of view of chiral MHD, the value of  $\mu_0$  (to which this bound is proportional) is just an initial condition and therefore can take arbitrary values. Once an initial condition with a large value of  $\mu_0$  has been generated, the subsequent evolution (as described above) does not require any new physics.

Moreover, the coupled evolution of magnetic helicity and chiral chemical potential is *unavoidable* in the relativistic plasma and should be an integral part of relativistic MHD (as was discussed in Paper I).

## 6.2. Proto-neutron stars and the CME

In this section we explore whether the CME and chiral dynamos can play a role in the development of strong magnetic fields in neutron stars. A proto-neutron star (PNS) is a stage of stellar evolution after the supernova core collapse and before the cold and dense neutron star is formed (see e.g. Pons et al. 1999). PNS are characterized by high temperatures (typically  $k_B T \sim \mathcal{O}(10) \text{ MeV} \gg m_e c^2$ ), large lepton number density (electron's Fermi energy  $\mu_e \sim$  few hundreds of MeV), presence of turbulent flows in the interior, and quickly changing environments. Once the formation of a neutron star is completed, its magnetic field can be extremely large. Neutron stars that exceed the quantum electrodynamic limit  $B_{\text{QED}} \equiv m_e^2 c^3 / (e \hbar) \approx 4.4 \times 10^{13} \text{ G}$  are known as “magnetars” (see, e.g., Mereghetti et al. 2015; Turolla et al. 2015; Kaspi & Beloborodov 2017, for recent reviews). The origin of such strong magnetic fields remains unknown, although many explanations have been proposed; see e.g. Duncan & Thompson (1992); Ferrario & Wickramasinghe (2006); Akiyama et al. (2003).

The role of the CME in the physics of (proto)neutron stars and their contribution to the generation of strong magnetic fields have been discussed in a number of works (Charbonneau & Zhitnitsky 2010; Ohnishi & Yamamoto 2014; Dvornikov & Semikoz 2015b,c; Yamamoto 2016; Grabowska et al. 2015; Sigl & Leite 2016; Dvornikov 2016).

### 6.2.1. Chiral MHD in proto-neutron stars

During the formation of a PNS, electrons and protons are converted into neutrons, leaving behind left-handed neutrinos. This is known as the Urca process ( $e + p \rightarrow n + \nu_e$ ) (Haensel 1995). If the chirality-flipping timescale, determined by the electron's mass, is longer than the instability scale, the net chiral asymmetry in the proto-neutron star can lead to the generation of magnetic fields. This scenario has been discussed previously (Ohnishi & Yamamoto 2014; Sigl & Leite 2016; Grabowska et al. 2015). The chiral turbulent dynamos discussed in this work can be relevant for the physics of PNS and can affect our conclusions about the importance of the CME. However, to make a detailed quantitative analysis, a number of factors should be taken into account:

(1) The rate of the Urca process is strongly temperature dependent (Lattimer et al. 1991; Haensel 1995). The temperatures inside PNSs are only known with large uncertainties and the cooling occurs on a scale of seconds (see e.g. Pons et al. 1999), making estimates of the Urca rates uncertain by orders of magnitude.

(2) The chirality flipping rate that aims to restore the depleted population of left-chiral electrons is also expected to be temperature dependent (see e.g. Grabowska et al. 2015; Sigl & Leite 2016).

(3) The neutrinos produced via the Urca process are trapped in the interior of a PNS and can release the chiral asymmetry back into the plasma via the  $n + \nu_e \rightarrow e + p$  process. Therefore, only when the star becomes transparent to neutrinos (as temperature drops to a few MeV), the creation of chiral asymmetry can become significant.

Modeling the details of PNS cooling and neutrino propagation is beyond the scope of this paper. Below we perform the estimates that demonstrate that chiral MHD can significantly change the picture of the evolution of a PNS.

### 6.2.2. Estimates of the relevant parameters

An upper limit of the chiral chemical potential can be estimated by assuming that  $n_L = 0$  and  $n_R = n_e$  (all left-chiral electrons have been converted into neutrinos and the rate of chirality flipping is much slower than other relevant processes). This leads to the estimate  $\mu_5 \simeq \mu_e$  and correspondingly

$$\mu_{\text{max}} = 4\alpha_{\text{em}} \frac{\mu_e}{\hbar c} = 4 \times 10^{11} \text{ cm}^{-1} \left( \frac{\mu_e}{250 \text{ MeV}} \right), \quad (60)$$

where we have used a typical value of the electron's Fermi energy  $\mu_e$  (Pons et al. 1999). For an ultra-relativistic degenerate electron gas (i.e. when  $\mu_e \gg k_B T \gg m_e c^2$ ) the relation between the number density of electrons,  $n_e$ , and their Fermi energy,  $\mu_e$ , is

$$\mu_e = \hbar c (2\pi^2 n_e)^{1/3} \approx 250 \text{ MeV} \left( \frac{n_e}{10^{38} \text{ cm}^{-3}} \right)^{1/3}. \quad (61)$$

The interior of neutron stars is a conducting medium whose conductivity is estimated to be (Baym et al. 1969; Kelly 1973):

$$\begin{aligned} \sigma(T) &= \sqrt{3} \left( \frac{4}{\pi} \right)^{3/2} \frac{\hbar^4 c^2}{e m_p^{3/2} k_B^2 T^2} n_e^{3/2} \\ &\approx 1 \times 10^{27} \left( \frac{1 \text{ MeV}}{k_B T} \right)^2 \left( \frac{n_e}{10^{38} \text{ cm}^{-3}} \right)^{3/2} \text{ s}^{-1} \end{aligned} \quad (62)$$

(there is actually a difference in the numerical coefficient  $\mathcal{O}(1)$  between the results of Baym et al. (1969) and Kelly (1973)). Using Equation (63), we find the magnetic diffusion coefficient as

$$\eta(T) \approx 7 \times 10^{-8} \text{ cm}^2 \text{ s}^{-1} \left( \frac{k_B T}{1 \text{ MeV}} \right)^2 \left( \frac{10^{38} \text{ cm}^{-3}}{n_e} \right)^{3/2}. \quad (64)$$

Therefore, we can determine the maximal rate of the small-scale chiral instability (26) as

$$\gamma_\mu^{\text{max}} = \frac{\mu_{\text{max}}^2 \eta}{4} = 2 \times 10^{15} \text{ s}^{-1} \left( \frac{\mu_e}{250 \text{ MeV}} \right)^2 \left( \frac{k_B T}{1 \text{ MeV}} \right)^2. \quad (65)$$

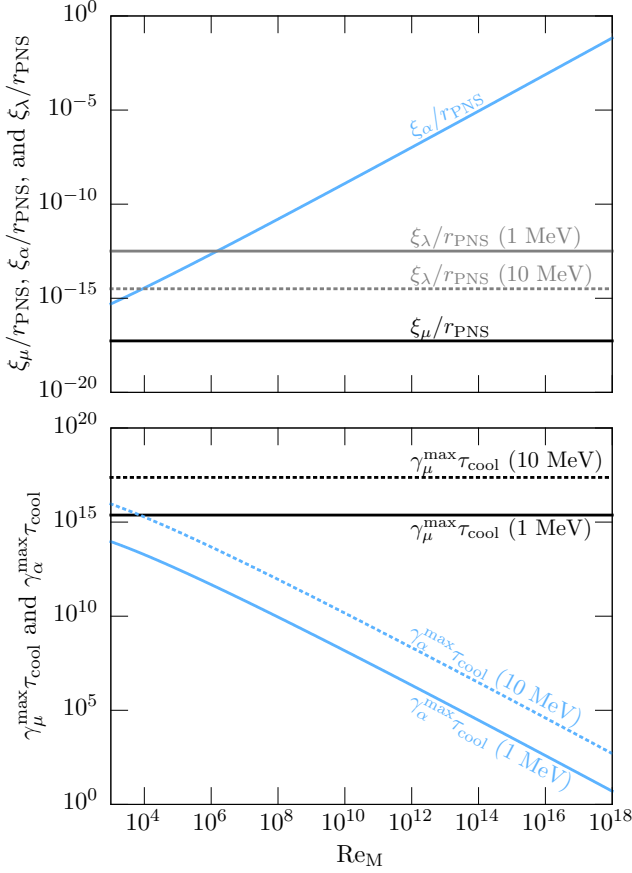


FIG. 20.— **Chiral MHD dynamos in PNS.** Laminar and turbulent growth rate multiplied by the cooling timescale (top panel) and the characteristic scales of chiral MHD normalized by the typical radius of the PNS  $r_{\text{NS}} \sim 10 \text{ km}$  (bottom panel). The estimates are presented as a function of  $\text{Re}_M$ . The initial value of the chiral chemical potential is assumed at the level (60) and the we use  $\mu_e = 250 \text{ MeV}$ . Since the conductivity is temperature dependent the ratios including  $\eta$  are presented for both,  $k_B T = 1 \text{ MeV}$  and  $k_B T = 10 \text{ MeV}$ .

We see that over a characteristic time  $\tau_{\text{cool}} \sim 1 \text{ s}$  (the typical cooling time), the magnetic field would increase by many  $e$ -foldings.

As in Section 6.1.1, the phase of the small-scale instability ends when turbulence is excited. It should be stressed, however, that unlike the early Universe, the interiors of PNS are expected to be turbulent with high  $\text{Re}_M$  even in the absence of chiral effects (with  $\text{Re}_M$  as large as  $10^{17}$ ); see Thompson & Duncan (1993). Therefore, the system may find itself in the forced turbulence regime of Section 5.2. Figure 20 shows that in a wide range of magnetic Reynolds numbers, one can have many  $e$ -foldings over a typical time scales of the PNS and that the scale of the magnetic field can reach macroscopic size.

### 6.2.3. Estimate of magnetic field strengths

A dedicated analysis, taking into account temperature and density evolution of the PNS as well as its turbulent regimes is needed to make detailed predictions. Here we will make the estimates of the strength of the magnetic field, similar to Section 6.1 above. To this end we use the conservation law (10), assuming  $\mu_0 = \mu_{\text{max}}$ . In the PNS case, the plasma is degenerate and therefore the relation

between  $n_5$  and  $\mu_5$  is given by

$$n_5 = \frac{\mu_5}{3\pi^2} (3\mu_e^2 + \pi^2 T^2) \quad (66)$$

(in the limit  $\mu_5 \ll T$ ). As a result, the chiral feedback parameter  $\lambda$  is

$$\lambda_{\text{PNS}} = \frac{\hbar c \pi^2}{2} \left( \frac{8\alpha_{\text{em}}}{\mu_e} \right)^2, \quad (67)$$

which determines the wavenumber  $k_\lambda$ ; see Equation 20. The corresponding length scale  $\xi_\lambda = k_\lambda^{-1}$  is presented in the top panel of Figure 20, where we assume a mean density of the PNS of  $\bar{\rho}_{\text{PNS}} = 2.8 \times 10^{14} \text{ g cm}^{-3}$ .

Using Equations (60) and (67), we find

$$(B^2 \xi)_{\text{max}} = \frac{4\pi \mu_{\text{max}}}{\lambda_{\text{PNS}}} = \frac{\mu_e^3}{2(\hbar c)^2 \alpha_{\text{em}}} \quad (68)$$

$$\approx 1.4 \times 10^{24} \text{ G}^2 \text{ cm} \left( \frac{\mu_e}{250 \text{ MeV}} \right)^3. \quad (69)$$

Assuming for the maximal correlation scale  $\xi_{\text{PNS}} \sim 1 \text{ cm}$  (see Figure 20), we find that magnetic field strength is of the order of

$$B_{\text{max}} \sim 1.2 \times 10^{12} \text{ G} \left( \frac{\mu_e}{250 \text{ MeV}} \right)^{3/2} \left( \frac{1 \text{ cm}}{\xi_M} \right)^{1/2}. \quad (70)$$

Notice that the estimate (68) is independent of  $T$  (but depends strongly on the assumed value of  $\mu_e$ ).

Our estimates have demonstrated that the chiral MHD could be capable of generating strong small-scale magnetic fields. *Therefore, chiral effects should be included in the modeling of evolution of proto-neutron stars.*

## 7. CONCLUSIONS

In this work we have presented results of numerical simulations of chiral MHD, that include the temporal and spatial evolution of magnetic fields, plasma motions, and the chiral chemical potential. The chiral magnetic effect (CME) caused by an asymmetry between left- and right-handed fermions in a relativistic plasma with a magnetic field, results in excitation of a small-scale chiral dynamo instability.

With our numerical simulations, we confirm various theoretical predictions of the laminar and turbulent large-scale dynamos discussed in Paper I. The chiral dynamo amplifies a weak seed magnetic field with a growth rate that depends on the chiral velocity  $v_\mu$ , the shear  $S$  of the imposed nonuniform plasma motions, and the fluid and magnetic Reynolds numbers of the turbulence that is chiral magnetically or externally driven.

The main findings presented in this paper are the following:

- For the laminar chiral and chiral–shear dynamos, the maximum growth rate of the magnetic field becomes larger in the presence of an imposed shearing motion, and in the limit of large shear, the growth rate of the  $v_\mu$ –shear dynamo scales with shear as  $S^{2/3}$ . The magnetic field saturates, in accordance with the conservation law for the total chirality at a value proportional to  $\lambda^{-1/2}$ .

- The CME can drive turbulence efficiently via the Lorentz force. This is indicated by the measured growth rate of turbulent velocity which is approximately a factor of two larger than that of the magnetic field.
- In the presence of small-scale turbulence, the large-scale dynamo operates due to the chiral  $\alpha_\mu$  effect that is not related to the mean kinetic helicity, and the dynamo growth rate is close to the prediction of mean-field chiral MHD for both, chiral magnetically produced turbulence as well as for externally driven turbulence.

Using DNS we found a new scenario of the magnetic field evolution consisting of three phases:

- (1) small-scale chiral dynamo instability;
- (2) production of small-scale turbulence, inverse transfer of magnetic energy, and generation of a large-scale magnetic field by the chiral  $\alpha_\mu$  effect;
- (3) saturation of the large-scale chiral dynamo by a decrease of the CME controlled by the conservation law for the total chirality:  $\lambda \langle \mathbf{A} \cdot \mathbf{B} \rangle / 2 + \langle \mu \rangle = \mu_0$ .

The previously discussed scenario of magnetic field evolution caused by the CME (Boyersky et al. 2012) did not include the second phase.

While the results summarized above have been obtained in simulations of well resolved periodic domains, astrophysical parameters are beyond the regime accessi-

ble to DNS. Hence we can only estimate the effects of the chiral anomaly in relativistic astrophysical plasmas, like in the early Universe or in neutron stars. Our estimates for magnetic fields produced by chiral dynamos in the early Universe are roughly consistent with the observational lower limits found by Dermer et al. (2011), if we assume a large chiral chemical potential. In proto-neutron stars, chiral dynamos operating in the first tens of seconds after the supernova explosion, can produce magnetic fields of approximately  $10^{12}$  G at a magnetic correlation length of 1 cm.

We acknowledge support from *Nordita*, which is funded by the Nordic Council of Ministers, the Swedish Research Council, and the two host universities, the *Royal Institute of Technology* (KTH) and *Stockholm University*. This project has received funding from the European Union's Horizon 2020 research and innovation programme under the Marie Skłodowska-Curie grant No. 665667. Support through the NSF Astrophysics and Astronomy Grant Program (grants 1615100 & 1615940), the Research Council of Norway (FRINATEK grant 231444), and the European Research Council (grant number 694896) are gratefully acknowledged. Simulations presented in this work have been performed with computing resources provided by the Swedish National Allocations Committee at the Center for Parallel Computers at the Royal Institute of Technology in Stockholm.

## REFERENCES

- Akiyama, S., Wheeler, J. C., Meier, D. L., & Lichtenstadt, I. 2003, *ApJ*, 584
- Alekseev, A. Y., Cheianov, V. V., & Fröhlich, J. 1998, *Phys. Rev. Lett.*, 81, 3503
- Arnold, P., Moore, G. D., & Yaffe, L. G. 2000, *J. High Energy Phys.*, 11, 001
- Artsimovich, L. A., & Sagdeev, R. Z. 1985, *Plasma Physics for Physicists* (Benjamin, New York)
- Banerjee, R., & Jedamzik, K. 2004, *Phys. Rev. D*, 70, 123003
- Baym, G., Bödeker, D., & McLerran, L. 1996, *Phys. Rev. D*, 53
- Baym, G., Pethick, C., & Pikes, D. 1969, *Nature*, 224, 674
- Beck, R. 2016, *A&A Rev.*, 24
- Bell, A. R. 2004, *MNRAS*, 353, 550
- Beresnyak, A., & Li, H. 2014, *ApJ*, 788, 107
- Biskamp, D. 1997, *Nonlinear Magnetohydrodynamics*, Cambridge monographs on plasma physics (Cambridge University Press)
- Biskamp, D., & Müller, W.-C. 1999, *Phys. Rev. Lett.*, 83
- Boyersky, A., Fröhlich, J., & Ruchayskiy, O. 2012, *Phys. Rev. Lett.*, 108
- . 2015, *Phys. Rev. D*, 92, 043004
- Brandenburg, A. 2003, *Computational aspects of astrophysical MHD and turbulence* (CRC Press), 269344
- Brandenburg, A., & Dobler, W. 2002, *Comp. Phys. Comm.*, 147, 471, [astro-ph/0111569](#)
- Brandenburg, A., Enqvist, K., & Olesen, P. 1996, *Phys. Rev. D*, 54
- Brandenburg, A., & Kahnishvili, T. 2017, *Phys. Rev. Lett.*, 118, 055102, [1607.01360](#)
- Brandenburg, A., Rädler, K.-H., & Schrunner, M. 2008, *A&A*, 482, 739
- Brandenburg, A., Schober, J., & Rogachevskii, I. 2017a, *Astron. Nachr.*, 338, 790
- Brandenburg, A., Schober, J., Rogachevskii, I., Kahnishvili, T., Boyarsky, A., Fröhlich, J., Ruchayskiy, O., & Kleorin, N. 2017b, *ApJL*, 845, L21, [1707.03385](#)
- Brandenburg, A., & Subramanian, K. 2005, *Phys. Rept.*, 417, 1
- Caprini, C., Durrer, R., & Fenu, E. 2009, *JCAP*, 0911, 001, [0906.4976](#)
- Charbonneau, J., & Zhitnitsky, A. 2010, *JCAP*, 1008, 010, [0903.4450](#)
- Charbonneau, P. 2014, *ARA&A*, 52, 251
- Christensson, M., Hindmarsh, M., & Brandenburg, A. 2001, *Phys. Rev. E*, 64
- Crutcher, R. M. 2012, *ARA&A*, 50
- Davidson, S. 1996, *Phys. Lett. B*, 380, 253, [astro-ph/9605086](#)
- Dermer, C. D., Cavadini, M., Razzaque, S., Finke, J. D., Chiang, J., & Lott, B. 2011, *ApJ*, 733, L21
- Dolag, K., Kachelriess, M., Ostapchenko, S., & Tomas, R. 2011, *ApJ*, 727, L4, [1009.1782](#)
- Donati, J.-F., & Landstreet, J. D. 2009, *ARA&A*, 47, 333
- Duncan, R. C., & Thompson, C. 1992, *ApJ*, 392
- Durrer, R., & Caprini, C. 2003, *JCAP*, 0311, 010, [astro-ph/0305059](#)
- Durrer, R., & Neronov, A. 2013, *A&A Rev.*, 21, 62
- Dvornikov, M. 2016, [1612.06540](#)
- Dvornikov, M., & Semikoz, V. B. 2015a, *Phys. Rev. D*, 92, 083007
- . 2015b, *JCAP*, 1505, 032, [1503.04162](#)
- . 2015c, *Phys. Rev. D*, 91, 061301
- . 2017, *Phys. Rev. D*, 95, 043538
- Enqvist, K. 1994, in *1st International Conference on Strong and Electroweak Matter (SEWM 1994)* Sintra, Portugal, March 23-25, 1994, 143-154, [hep-ph/9405315](#)
- Enqvist, K., & Olesen, P. 1993, *Phys. Lett. B*, 319, 178, [hep-ph/9308270](#)
- Ferrario, L., & Wickramasinghe, D. 2006, *MNRAS*, 367, 1323
- Fröhlich, J., & Pedrini, B. 2000, in *Mathematical Physics 2000*, ed. A. S. Fokas, A. Grigoryan, T. Kibble, & B. Zegarlinski, International Conference on Mathematical Physics 2000, Imperial college (London) (World Scientific Publishing Company)
- Fröhlich, J., & Pedrini, B. 2002, in *Statistical Field Theory*, ed. A. Cappelli & G. Mussardo (Kluwer)
- Fukushima, K., Kharzeev, D. E., & Warringa, H. J. 2008, *Phys. Rev. D*, 78, 074033
- Gasperini, M., Giovannini, M., & Veneziano, G. 1995, *Phys. Rev. Lett.*, 75, 3796
- Giovannini, M. 2004, *Int. J. Mod. Phys. D*, 13, 391, [astro-ph/0312614](#)
- Giovannini, M., & Shaposhnikov, M. E. 1998, *Phys. Rev. D*, 57, 2186, [hep-ph/9710234](#)



- Grabowska, D., Kaplan, D. B., & Reddy, S. 2015, *Phys. Rev. D*, 91, 085035
- Grasso, D., & Rubinstein, H. R. 2001, *Phys. Rep.*, 348, 163
- Haensel, P. 1995, *Space Sci. Rev.*, 74, 427
- Haugen, N. E., Brandenburg, A., & Dobler, W. 2004, *Phys. Rev. E*, 70, 016308
- Hirono, Y., Kharzeev, D., & Yin, Y. 2015, *Phys. Rev. D*, 92, 125031, 1509.07790
- Joyce, M., & Shaposhnikov, M. 1997, *Phys. Rev. Lett.*, 79, 1193
- Kahniashvili, T., Maravin, Y., Natarajan, A., Battaglia, N., & Tevzadze, A. G. 2013a, *ApJ*, 770, 47
- Kahniashvili, T., Tevzadze, A. G., Brandenburg, A., & Neronov, A. 2013b, *Phys. Rev. D*, 87, 083007
- Kaspi, V. M., & Beloborodov, A. M. 2017, *ARA&A*, 55
- Kelly, D. C. 1973, *ApJ*, 179, 599
- Krause, F., & Rädler, K. H. 1980, *Mean-Field Magnetohydrodynamics and Dynamo Theory* (Pergamon, Oxford)
- Kulsrud, R. M., & Zweibel, E. G. 2008, *Rep. Prog. Phys.*, 71, 046901
- Lattimer, J. M., Prakash, M., Pethick, C. J., & Haensel, P. 1991, *Phys. Rev. Lett.*, 66, 2701
- Melrose, D. 2012, *Quantum Plasmadynamics: Magnetized Plasmas*, *Lecture Notes in Physics* (Springer New York)
- Mereghetti, S., Pons, J. A., & Melatos, A. 2015, *Space Sci. Rev.*, 191, 315
- Moffatt, H. K. 1978, *Magnetic Field Generation in Electrically Conducting Fluids* (Cambridge, England, Cambridge University Press)
- Neronov, A., & Vovk, I. 2010, *Science*, 328, 73
- Ohnishi, A., & Yamamoto, N. 2014, 1402.4760
- Olesen, P. 1992, *Phys. Lett. B*, 281, 300
- Pandey, K. L., Choudhury, T. R., Sethi, S. K., & Ferrara, A. 2015, *MNRAS*, 451, 1692
- Parker, E. 1979, *Cosmical Magnetic Fields* (Oxford University Press, New York)
- Parker, E. N. 1955, *ApJ*, 122, 293
- Pavlović, P., Leite, N., & Sigl, G. 2017, *Phys. Rev. D*, 96, 023504, 1612.07382
- Pons, J. A., Reddy, S., Prakash, M., Lattimer, J. M., & Miralles, J. A. 1999, *ApJ*, 513, 780
- Redlich, A. N., & Wijewardhana, L. C. R. 1985, *Phys. Rev. Lett.*, 54, 970
- Rees, M. J. 1987, *Q. J. R. Astron. Soc.*, 28, 197
- Reiners, A. 2012, *Liv. Rev. Sol. Phys.*, 9, 1
- Rogachevskii, I., Kleeorin, N., Brandenburg, A., & Eichler, D. 2012, *ApJ*, 753, 6
- Rogachevskii, I., Ruchayskiy, O., Boyarsky, A., Fröhlich, J., Kleeorin, N., Brandenburg, A., & Schober, J. 2017, *ApJ*, 846, 153, 1705.00378
- Saveliev, A., Jedamzik, K., & Sigl, G. 2012, *Phys. Rev. D*, 86, 103010, 1208.0444
- Semikoz, V., Sokoloff, D., & Valle, J. 2012, *JCAP*, 1206, 008, 1205.3607
- Semikoz, V. B. 2010, in *Proceedings, 14th Lomonosov Conference on Elementary Particle Physics (LomCon): Moscow, Russia, August 19-25, 2009*, 259–261
- Sigl, G., & Leite, N. 2016, *JCAP*, 1, 025
- Sigl, G., & Leite, N. 2016, *JCAP*, 1601, 025, 1507.04983
- Sigl, G., Olinto, A. V., & Jedamzik, K. 1997, *Phys. Rev. D*, 55, 4582
- Son, D. T., & Surowka, P. 2009, *Phys. Rev. Lett.*, 103, 191601
- Subramanian, K. 2016, *Rep. Prog. Phys.*, 79, 076901
- Tashiro, H., Vachaspati, T., & Vilenkin, A. 2012, *Phys. Rev. D*, 86, 105033
- Tavecchio, F., et al. 2010, *MNRAS*, 406, L70, 1004.1329
- Thompson, C., & Duncan, R. C. 1993, *ApJ*, 408, 194
- Tsokos, K. 1985, *Phys. Lett. B*, 157, 413
- Turner, M. S., & Widrow, L. M. 1988, *Phys. Rev. D*, 37, 2743
- Turolla, R., Zane, S., & Watts, A. L. 2015, *Rep. Prog. Phys.*, 78, 116901
- Vachaspati, T. 1991, *Phys. Lett. B*, 265, 258
- . 2001, *Phys. Rev. Lett.*, 87, 251302
- Vachaspati, T., & Field, G. B. 1994, *Phys. Rev. Lett.*, 73, 373, [hep-ph/9401220](#)
- Vilenkin, A. 1979, *Phys. Rev. D*, 20, 1807
- . 1980, *Phys. Rev. D*, 22, 3080
- Widrow, L. M. 2002, *Rev. Mod. Phys.*, 74, 775, [astro-ph/0207240](#)
- Widrow, L. M., Ryu, D., Schleicher, D. R. G., Subramanian, K., Tsagas, C. G., & Treumann, R. A. 2012, *Space Sci. Rev.*, 166, 37
- Yamamoto, N. 2016, *Phys. Rev. D*, 93, 065017, 1511.00933
- Zeldovich, Y. B., Ruzmaikin, A. A., & Sokoloff, D. D. 1983, *Magnetic Fields in Astrophysics (Gordon and Breach, New York)*